42

SATELLITE & MESOMETEOROLOGY RESEARCH PROJECT

Department of the Geophysical Sciences
The University of Chicago

A STUDY OF FACTORS CONTRIBUTING TO DISSIPATION OF ENERGY IN A DEVELOPING CUMULONIMBUS

Rodger A. Brown and Tetsuya Fujita

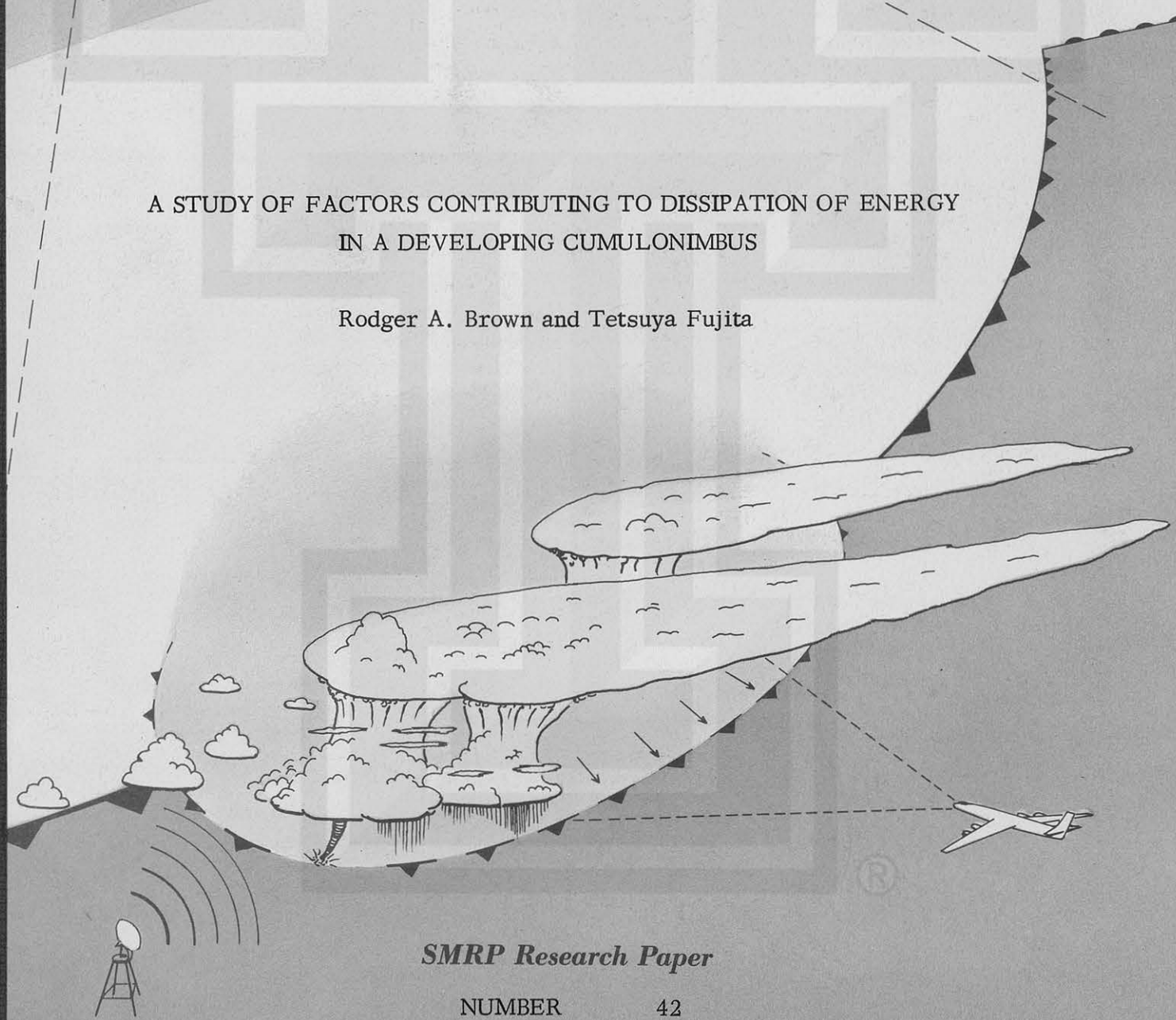

SMRP Research Paper

NUMBER 42

May 1965

MESOMETEOROLOGY PROJECT ---- RESEARCH PAPERS

1.* Report on the Chicago Tornado of March 4, 1961 - Rodger A. Brown and Tetsuya Fujita

2.* Index to the NSSP Surface Network - Tetsuya Fujita

3.* Outline of a Technique for Precise Rectification of Satellite Cloud Photographs - Tetsuya Fujita

4.* Horizontal Structure of Mountain Winds - Henry A. Brown

5.* An Investigation of Developmental Processes of the Wake Depression Through Excess Pressure Analysis of Nocturnal Showers - Joseph L. Goldman

6.* Precipitation in the 1960 Flagstaff Mesometeorological Network - Kenneth A. Styber

7.** On a Method of Single- and Dual-Image Photogrammetry of Panoramic Aerial Photographs - Tetsuya Fujita

8. A Review of Researches on Analytical Mesometeorology - Tetsuya Fujita

9. Meteorological Interpretations of Convective Nephsystems Appearing in TIROS Cloud Photographs - Tetsuya Fujita, Toshimitsu Ushijima, William A. Hass, and George T. Dellert, Jr.

10. Study of the Development of Prefrontal Squall-Systems Using NSSP Network Data - Joseph L. Goldman

11. Analysis of Selected Aircraft Data from NSSP Operation, 1962 - Tetsuya Fujita

12. Study of a Long Condensation Trail Photographed by TIROS I - Toshimitsu Ushijima

13. A Technique for Precise Analysis of Satellite Data; Volume I - Photogrammetry (Published as MSL Report No. 14) - Tetsuya Fujita

14. Investigation of a Summer Jet Stream Using TIROS and Aerological Data - Kozo Ninomiya

15. Outline of a Theory and Examples for Precise Analysis of Satellite Radiation Data - Tetsuya Fujita

* Out of print
** To be published

(Continued on back cover)

SATELLITE AND MESOMETEOROLOGY RESEARCH PROJECT
Department of the Geophysical Sciences
The University of Chicago

A STUDY OF FACTORS CONTRIBUTING TO DISSIPATION OF ENERGY IN A DEVELOPING CUMULONIMBUS

by

Rodger A. Brown and Tetsuya Fujita

SMRP Research Paper # 42

May 1965

The research reported in this paper has been partially supported by the Air Force, under contract AF 19(604)-7259 and partially by the U. S. Weather Bureau, National Severe Storms Laboratory, under grant CWB WBG - 41.

A STUDY OF FACTORS CONTRIBUTING TO DISSIPATION OF ENERGY IN A DEVELOPING CUMULONIMBUS

Rodger A. Brown and Tetsuya Fujita

Department of the Geophysical Sciences
The University of Chicago
Chicago, Illinois

ABSTRACT

This study is concerned with an orographic cumulonimbus that developed near Flagstaff, Arizona on 19 July 1960. The growth of small cumuli into the cumulonimbus and the expansion of the latter's top were investigated using stereo-pair photographs. The photogrammetric analysis revealed that the growth of the cumulus congestus stage was characterized by a series of pulsations, each attaining greater heights than the previous one. The analysis of the anvil top revealed that it was rotating cyclonically as it expanded - an indication that the entire thunderstorm was rotating in the same sense, with vorticity values of up to 10^{-2}sec^{-1} or greater. At the time that the cumulonimbus was developing an anvil, aircraft temperature measurements were made at 11.3 km in the region surrounding both this storm and one that had developed about half an hour earlier. The temperature consistently increased by about 1.5C in 70 km as the clouds were approached from the downwind side. The heating was interpreted as being due to the dry-adiabatic subsidence of air passing out through the anvils (12.6 km). Equations are developed, using the entrainment technique, for determining temperature, liquid-water content, kinetic energy, vertical and radial components of velocity, and hydrostatic and non-hydrostatic parts of the pressure. However, in combining the vertical velocity from a proximity rawinsonde observation and the updraft suggested by the rate of anvil expansion, it was necessary to introduce a three-region model for a developing cumulonimbus (updraft stage). This model produced a realistic distribution of the various meteorological parameters, which among other things resulted in a 0.8 mb low pressure area existing in the convergent region beneath the cloud. By taking advantage of the equivalence of the entrainment concept and turbulent exchange processes, it was possible to use the kinetic energy and vertical and radial velocity data to compute the kinematic eddy viscosity coefficient throughout the vertical stem of the cumulonimbus. The values, which ranged from 10^2 to 10^4 m^2 sec^{-1}, agree with those computed from a set of theoretical equations recently proposed by Brown (1965).

The research reported in this paper has been partially supported by the Air Force, under contract AF 19(604)-7259 and partially by the U. S. Weather Bureau, National Severe Storms Laboratory, under grant CWB WBG - 41.

1. Introduction

Due to the complexities involved in the dynamics of vertical motions in convective clouds, the dynamics have long been treated from a hydrostatic point of view. The "parcel method," with its non-interaction with the environment, has been used as a crude first approximation to convective processes. In order to satisfy continuity requirements the "slice method" was introduced by Bjerknes (1938) and has since been slightly modified by others.

Even though the idea can be found in earlier literature, it was not until 1947 that the concept of cumulus modification by the lateral entrainment of environmental air was clearly set forth. Using theoretical and empirical considerations, respectively, Schmidt (1947) in Holland and Stommel (1947) in the United States independently showed that entrainment should occur. This was followed by theoretical studies (Austin, 1948; Austin and Fleisher, 1948; Houghton and Cramer, 1951; Stommel , 1951; and others) which showed the influence of various environmental conditions on ascending masses of either cloudy or non-saturated air. Subsequent investigators (Bunker, 1953; Dufour, 1956a and b; Haltiner, 1959; Haltiner and Chase, 1960; Mason and Emig, 1961; Squires and Turner, 1962; Lilly, 1962; Chou, 1962; Ogura, 1963; Malkus and Williams, 1963; and others) have included in their theoretical studies such sources of energy dissipation as liquid-water drag, form drag, eddy diffusion, and eddy viscosity. However, as pointed out by Kuo (1962), the entrainment concept is simply a manifestation of the turbulent exchange processes (eddy diffusion and viscosity).

Entrainment is a simple graphical procedure and, as discussed later, a characteristic entrainment rate can be computed for a given sized cloud. However, when one attempts to determine the proper order of magnitude of the exchange coefficients, as, for example, in the numerical simulation of a growing cumulus, there has been no definite solution to the problem; most investigators have assumed that the coefficients are arbitrary constants. Recently, Brown (1965) proposed a set of equations for evaluating the exchange coefficients from a three-dimensional wind field; but his equations have not yet been tested by using actual data.

Richardson (1921) and Ogura (1963) have published "computed" estimates of one of the exchange coefficients for cumuli and cumulonimbi, respectively. Their estimates were for the eddy viscosity coefficient; they obtained values of 10^2 and $10^3 m^2 sec^{-1}$ for small cumuli and cumulonimbi, respectively. Instead of having just one eddy viscosity coefficient, Brown (1965) has suggested that there should be three -

one for each wind-component direction. Using a simplified model to evaluate his eddy viscosity coefficient for vertical motion, he concluded that Richardson's estimate was reasonable as a mean value for cumuli but that Ogura's estimate was too low for a well-developed cumulonimbus.

Many writers (Christians, 1935; Schmidt, 1947; Gutman, 1961; Chou, 1962; Lilly, 1962; Ogura, 1963; and others) have intuitively expressed what they felt the order of magnitude should be for the eddy viscosity coefficient in cumulus clouds. Their estimates range from 1 to 10^2 m^2 sec^{-1}, with the order of 10^2 m^2 sec^{-1} being the most prevalent.

The primary purpose of this paper is to investigate the various factors that lead to the dissipation of energy in a cumulonimbus and then to obtain empirically the order of magnitude of the eddy viscosity coefficient for a developing cumulonimbus. Computed values of the coefficient will then be compared with those obtained from Brown's theoretical equations.

The study is based on rawinsonde observations and stereophotogrammetric data of a cumulonimbus that occurred near Flagstaff, Arizona on 19 July 1960. In order to successfully combine the rawinsonde and photogrammetric data, a three-region model for a cumulonimbus (prior to the formation of any downdrafts) is introduced. This procedure leads to a realistic distribution of vertical and radial velocities within the cloud. The vertical velocities, which are obtained by applying the entrainment concept, are then used as initial data for computing the eddy viscosity coefficient; this utilizes the fact that the entrainment concept and turbulent exchange processes are synonymous.

Additional aspects of a developing cumulonimbus will also be mentioned; brief evidence will be presented to show that cumulonimbus was slowly rotating in a counter-clockwise sense. Also the hydrostatic and non-hydrostatic components of the pressure will be evaluated and discussed.

2. Development of the Governing Equations

The equations developed in this section are to be used in conjunction with the rawinsonde and photogrammetric data that are presented later; rawinsonde data will be evaluated on an adiabatic chart.

Thermodynamic (entrainment) equations. In these thermodynamic equations, which are basically those presented by Stommel (1947), entrainment is evaluated in

a graphical manner after plotting the environmental sounding on an adiabatic chart. The entraining process can be divided into three steps. First, the cloud mass ascends moist adiabatically a vertical distance of Δp mb from level 1 (T_1, χ_{v_1}) to level 2 (T_2'', χ_{v_2}''), where T is temperature and χ_v is mixing ratio.

The second step involves a fractional increase ($\delta m/m$) of the original cloud mass (m) at level 2 due to the entrainment of environmental air (T_2^*, χ_{v2}^*). The sudden increase of mass at level 2 represents (in nature) a continual mass increase from level 1 to level 2, both of which result in the same increase of δm. As a result of this mixing, the temperature and mixing ratio of the cloud air are T_2' and χ_{v2}', respectively, as computed from

$$T_2' = \frac{T_2'' + T_2^* E \Delta p}{1 + E \Delta p} \qquad (1)$$

and

$$\chi_{v2}' = \frac{\chi_{v2}'' + \chi_{v2}^* E \Delta p}{1 + E \Delta p} , \qquad (2)$$

where: the star refers to an environmental value; the double prime represents the fictitious cloud value at the upper level prior to entrainment and after a moist adiabatic ascent of Δp mb; the single prime represents the fictitious cloud value after entrainment and before resaturating the air; $E = (1/m)\,\delta m/\delta p$ and is the entrainment rate, which is expressed in per cent per 100 mb.

In nearly all cases, χ_{v2}' is less than the saturated mixing ratio that T_2' would require in order for the cloud air to be saturated. This involves a third graphical step. The graphical procedure is to let the air having temperature T_2' ascend dry adiabatically (since the air is not saturated) until it intersects the mixing ratio line χ_{v2}'. The saturated air then descends moist adiabatically to level 2, where the final temperature and mixing ratio are T_2 and χ_{v2}, respectively. The final temperature is cooler than T_2' due to the heat that had to be removed from the air in order to evaporate the amount of liquid water (equal to $\chi_{v2} - \chi_{v2}'$) necessary to resaturate the air. A line drawn through T_1 and T_2 represents the actual lapse of temperature in the cloud as a result of the continuous entrainment of environmental air. The same three-step procedure is repeated for the following Δp ascents up to the top of the cloud (defined as the level at which the vertical velocity is equal to zero).

Continuity of water substances. Let χ_{l_1} represent the amount of liquid water (gm kg^{-1}) in the cloud at level 1. As the air ascends moist adiabatically the liquid-water content will increase by an amount equal to the decrease in the mixing ratio

$(\chi_{v_1}-\chi''_{v_2})$. During the entraining step, no liquid water is entrained. In fact, due to the dry entrained air, the liquid-water content will be reduced to $1/(1+E\Delta p)$ of its pre-entrainment value. Finally a certain amount $(\chi_{v_2}-\chi'_{v_2})$ of liquid water must be evaporated in order to resaturate the air. The liquid-water content of the cloud at level 2 can be computed from

$$\chi_{l2} = \frac{\chi_{l_1}+(\chi_{v_1}-\chi''_{v_2})}{1+E\Delta p} - (\chi_{v_2}-\chi'_{v_2}) \ . \qquad (3)$$

It will be noted that the assumption is made here that all of the liquid water is carried aloft and none leaves the ascending air in the form of precipitation.

Energy equation. In this paper, only changes in the vertical are considered; the only exception is the radial component of the motion which will be computed using the continuity equation. The energy equation will be developed from the vertical equation of motion. For a particular level in a cloud the equation can be written as

$$\frac{d}{dt}(\rho w) = -\frac{dp}{dz} - \rho g (1+\chi_l) \ , \qquad (4)$$

where ρ is the density of the cloud air, w is the vertical component of the velocity in the cloud (it is assumed that the vertical motion in the environment is negligible), p is the pressure in the cloud, g is the acceleration due to gravity, and χ_l is the cloud liquid-water content. If one makes use of the approximation that the vertical gradient of the pressure is the same within and outside the cloud and then assumes that the environment is in hydrostatic equilibrium, (4) becomes

$$\frac{d}{dt}(\rho w) = (\rho^*-\rho) g - \rho g \chi_l \ ,$$

where ρ^* is the density of the environmental air. Further expansion of the latter equation results in

$$\frac{dw}{dt} = \left(\frac{\rho^*-\rho}{\rho}\right) g - g\chi_l - \frac{w}{m}\frac{dm}{dt} \ ,$$

where both the numerator and denominator in the term on the extreme right have been multiplied by a volume of arbitrary magnitude. The three terms on the right side of the equation represent, in order, the buoyant acceleration, downward acceleration due to the weight of the liquid water, and the dissipation of the buoyant energy due to the turbulent mixing (entrainment) with the drier and more dense environmental air.

It is at this point that the equation can be approximated by graphical techniques. First of all, the entrainment term can be absorbed into the buoyancy term by using

the graphical techniques described at the beginning of this section. The effect of water vapor on the environmental density can be approximated by substituting the following expression for ρ^*

$$\rho^* = \frac{p}{R_d T_v^*} \quad , \tag{5}$$

where T_v^* is the virtual temperature of the environmental air and R_d is the gas constant for dry air. Similarly, the liquid-water drag can be taken into account by replacing ρ with an expression containing the liquid-water virtual temperature (T_{vw})

$$\rho = \frac{p}{R_d T_{vw}} \quad , \tag{6}$$

where T_{vw} (similar to a definition given by Fujita, 1951) can be approximated by

$$T_{vw} = T(1 + .61\chi_v - \chi_l) \quad . \tag{7}$$

In the absence of liquid water, this equation reduces to the conventional one for virtual temperature. After taking these various approximations into account, (4) finally becomes

$$\frac{dw}{dt} = \left(\frac{T_{vw} - T_v^*}{T_v^*}\right) g \quad . \tag{8}$$

The left side of (8) can be expanded as follows for axial symmetry:

$$\frac{dw}{dt} = \frac{\partial w}{\partial t} + v_r \frac{\partial w}{\partial r} + w \frac{\partial w}{\partial z} \quad ,$$

where v_r is the radial component of the velocity and r is the radial distance from the center of the cloud. In the early anvil stage of a cumulonimbus, the local time change ($\partial w / \partial t$) is approximately zero. In the same stage of growth, the radial and vertical gradients of w are of the same orders of magnitude, but the radial velocity is one order of magnitude less than the vertical velocity. Therefore, (8) can be written as follows after multiplying each side by the density:

$$\rho w \frac{\partial w}{\partial z} = \rho \left(\frac{T_{vw} - T_v^*}{T_v^*}\right) g \quad .$$

By approximating the partial derivative with the corresponding total derivative and integrating from level 1 to level 2, this becomes

$$\frac{1}{2}\rho_2 w_2^2 = \frac{1}{2}\rho_1 w_1^2 + \bar{\rho}\Delta K \ , \qquad (9)$$

where $\bar{\rho}$ is the mean density from level 1 to level 2 and where

$$\Delta K = \int_1^2 \left(\frac{T_{vw} - T_v^*}{T_v^*}\right) g \, dz \qquad (10)$$

is the change in the kinetic energy per unit mass of the cumulonimbus between levels 1 and 2; the integral can be evaluated graphically with a planimeter. It should be noted that (9) does not represent the growth of a cloud from one level to another but rather the changes in the kinetic energy from one level to the next within the cloud.

Equation (9) does not include the retarding effect of environmental air (with no vertical motion) being mixed with the ascending cloud air. In order to take this into account (9) must be modified as follows

$$\frac{1}{2}\rho_2 \ w_2^2 = \frac{\frac{1}{2}\rho_1 w_1^2 + \bar{\rho}\Delta K}{1 + E\Delta p} \ . \qquad (11)$$

This equation is used to compute the vertical velocity within the cloud in a series of entraining steps. This procedure involves the arbitrary choice of a realistic value for the vertical velocity at the base of the cloud.

Equation of continuity. If it is assumed that the atmosphere is incompressible, the equation of continuity is

$$\frac{\partial}{\partial r}(v_r \, r) + \frac{\partial}{\partial z}(w \, r) = 0. \qquad (12)$$

This equation is used to compute the radial velocity once the vertical velocity is known.

A condition for incompressibility of a gas is that the velocity of the gas must be much less than the speed of sound. This condition is expressed by the equation of Prandtl and Tietjens (1934) which states that

$$\rho = \rho_0 \left(1 - \frac{1}{2}\frac{w^2}{c^2} + \cdots\right),$$

where ρ_0 is the density of gas for zero velocity, w is the velocity (here taken as the vertical velocity), and c is the speed of sound. In order to have more than a one-percent difference between ρ and ρ_0, w must be at least 50 m sec^{-1}. Since velocities of this magnitude are found only in localized areas of the most violent

thunderstorms, the incompressibility assumption is quite valid.

3. Entrainment Calculations using a Weighted-Mean Sounding

Before the equations derived above are applied to the particular thunderstorm situation, they will be evaluated in order to study the general influence of turbulent mixing on such parameters as the water content, excess temperature, kinetic energy, and the approximate upper limit of cloud growth. The environmental conditions were obtained from a weighted-mean sounding for 1200 MST on 19 July 1960 at Flagstaff, Arizona. The sounding was computed from the only two rawinsonde observations made by U. S. Air Force personnel for that day; they were released at 0525 and 1406 MST.

The "weighted" sounding, plotted on a tephigram, is presented in Fig. 1, wherein the superadiabatic layer near 7 km is interpreted as being caused by evaporational cooling at the top of a cloud layer. The dashed extension of the temperature curve just above 200 mb, which was not used in determining the weighted sounding, was the temperature distribution at that level for the 1406 release; reference will be made to it later. Since the 1406 release ascended through the descending environment near the cumulonimbus, it has been assumed that the lapse rate for the 1200 weighted sounding requires no adjustment for environmental vertical motions; that is, the corrections incorporated in the slice method are built into the sounding data.

As mentioned above, there is an empirical relationship which produces the basis for determining a realistic entrainment rate. Adapting an expression given by Squires and Turner (1962) for an entraining jet model of a cumulonimbus, we have

$$E = \frac{4\alpha\beta}{D}, \qquad (13)$$

where D is the diameter of the updraft, α is a dimensionless entrainment constant, and $\beta\,(= -\delta z / \delta p)$ is a variable parameter that converts the entrainment rate from a function of height to one of pressure. The entrainment constant, α, represents the ratio between radial and vertical velocities. From laboratory experiments dealing with air jets (see, e. g., Morton, 1959; Ricou and Spalding, 1951), 0.1 seems to be a reasonable value for α. Due to the change of pressure with height, β ranges from about 1 km per 100 mb at the base level of most clouds to 3 km per 100 mb near the tops of thunderstorms.

For this study, the entrainment rates will be expressed in terms of per cent $(100\ mb)^{-1}$. Figure 2 shows a plot of Eq. (13) with the entrainment rate as a function of diameter; the wide band represents the range of values for β. Also presented in the figure are deduced entrainment rates for actual clouds: tradewind cumuli (Stommel, 1947; Malkus, 1954) and cumulonimbi (Byers and Hull, 1949, as evaluated by Fujita, 1963). From Fig. 2 one is able to estimate a reasonable entrainment rate for any sized cloud. The significance of the inverse relationship between the size of a cloud and its entrainment rate will be demonstrated below.

Before starting the actual computations for the cloud, the conventional parcel-method approach for finding the height of a cloud base was tested by comparing the results using the weighted sounding and stereophotogrammetric data. Keeping the potential temperature and mixing ratio constant, a parcel of air rising from the surface reaches its condensation level at 5.4 km msl; the elevation of the ground is 2.1 km. The results of stereophotogrammetric measurements indicated below show the base of the clouds to be at 5.3 km. At least in this one instance there is an amazing agreement between the two values.

Liquid-water content. Now turning to the growth of clouds in the environment depicted in Fig. 1, Eqs. (1) - (3) were evaluated in 50-mb steps from the cloud base (540 mb) to a point above the expected top of the clouds for each of the following entrainment rates: 0, 10, 20, 30, 50, 70, 90, 110, 150, and 200 per cent $(100\ mb)^{-1}$. The wide range of liquid-water contents that can be expected in various sized clouds is depicted in Fig. 3; actually the figure shows the water content, liquid and solid. The dry region between 7 and 8 km (see Fig. 1) shows up in the curves for 150 and 200 per cent $(100\ mb)^{-1}$. For larger clouds with smaller entrainment rates, environmental conditions exert a lesser influence on the water content. From the figure, one would expect thunderstorms to have 5 to 10 times the water content of small cumuli. Ackerman (1959) has shown from measurements in tropical cumuli that as a cloud becomes both taller and wider the mean liquid-water content increases.

It should be pointed out that, as originally conceived, an evaluation using one entrainment rate for the entire horizontal cross section of a cloud necessarily means that the resulting values are to be interpreted only as horizontal averages. Therefore, in order to compare the values in the figure with actual in-cloud measurements, it is desirable to know the spatial distribution of liquid water within a cloud. Unfortunately, most investigators indicate only the height at which the sample was taken (see, e.g., Diem, 1948; Weickmann and aufm Kampe, 1953; Squires, 1958).

However, there are some (see, e.g., Zaitsev, 1950; Mei Yuan, 1963) who present their data in such a way that isopleths of liquid-water content can be drawn for a vertical section through the center of the cloud; these are the ones that can be used most readily in such comparisons. Zaitsev (1950) and Mei-Yuan (1963) found that the average liquid-water content in cumulus humilis clouds reached a maximum just below the top of the cloud. However, in cumulus congestus, Zaitsev found the maximum to occur mid-way between the base and the top; the liquid water decreased at a slower rate above the maximum than it had increased below. In this respect, the curves in Fig. 3 have a reasonable shape and slope.

The curve for the vertical distribution of the average liquid-water content for zero entrainment is what has been referred to in the literature as the "adiabatic liquid-water content." There is some confusion among the investigators as to how the adiabatic liquid-water content is related to the measured values. But, it is generally agreed that the measured values average about one-quarter of the adiabatic values and that the maximum values can be several times greater than the adiabatic values in some cases (see Squires, 1962).

It is quite clear from Fig. 3 that the adiabatic liquid-water content is the limiting value of the average liquid-water content as the diameter of the cloud becomes increasingly large. Therefore, the average of measured liquid-water contents should always be less than the adiabatic liquid-water content, which discrepancy increases as the cloud-size decreases. This has been confirmed in a recent survey conducted by Squires (1962). Among the various investigators it is felt that the difference between adiabatic and average measured values is due to the turbulent mixing between a cloud and its environment; that this is the case has been demonstrated above. In short, it appears that the adiabatic liquid-water content is of assistance in determining the amount of mixing that takes place between a cloud and the surrounding air; consequently one is able to deduce the size of the cloud that was originally sampled.

Temperature. The liquid-water virtual temperature in the cloud is given by (7), which is repeated below:

$$T_{VW} = T(1 + .61X_V - X_L). \qquad (7)$$

As mentioned earlier in this section, the curves in Fig. 3 represent the total water content, both liquid and solid. In order to acknowledge the fact that super-cooled

water generally exists only at temperatures warmer than -40C, the following simplified scheme was set up: 1) for T_{VW} greater than 253K only liquid water is present in the cloud, 2) between 253K and 233K, there is a linear decrease of liquid water from 100 to 0 per cent and 3) less than 233K only solid water is present. This scheme is needed because the density of snow pellets and graupel is less than that of liquid water. Based on studies by List (1958) and Braham (1963) it appears that the density of solid water is about 0.85 that of liquid water. Therefore, this value was used in the χ_l term of (7) for computing the liquid-water virtual temperature at temperatures lower than 253K.

Equation (7) was evaluated for the same ten entrainment rates as for the water content. The excess temperature, ΔT, defined as

$$\Delta T = T_{VW} - T_V^*$$

was then computed from the temperatures. Figure 4 shows the excess temperature distribution for five entrainment rates: 0, 20, 50, 110, and 200 per cent $(100\ mb)^{-1}$. The dashed curve beneath the cloud is the excess temperature for rising air in which no turbulent mixing has taken place.

Kinetic energy. The kinetic energies per unit mass for the various entrainment rates were determined from (10). It was assumed that the mean vertical velocity at the base of the cloud increased from 2 to 8 m sec^{-1} as the entrainment rate decreased from 200 to 0 per cent $(100\ mb)^{-1}$. The resulting energy curves are shown in Fig. 5. The immediate conclusion to be drawn is that the entrainment of environmental air into a cloud has a pronounced effect on the energy that is available for cloud growth. An entrainment rate of only 20 per cent $(100\ mb)^{-1}$ cuts the maximum kinetic energy in half, as compared with the ideal case of zero entrainment. The 20 per cent value is cut in half again by an entrainment rate of 50 per cent $(100\ mb)^{-1}$. This clearly substantiates the statement made above that the larger the entrainment rate, the smaller the cloud and vice versa.

One notes that the tops of large cumulonimbi (in the environment shown in Fig. 1) should be found at a level about 12.5 km above sea level. Small cumuli having entrainment rates between 150 and 200 per cent $(100\ mb)^{-1}$ (diameters 0.2 to 1 km, according to Fig. 2) should grow up to about 7 km msl. In their photogrammetric study of small cumulus clouds (mean diameter about 1 km occurring earlier on the same day), Glass and Carlson (1963) found that the cloud thermals stopped growing after reaching average heights of 7.0 to 7.5 km. From Fig. 5 one might assume, therefore, that cumulus clouds larger than 1 km would quickly penetrate to the 9-km level, after which they would grow to thunderstorm proportions.

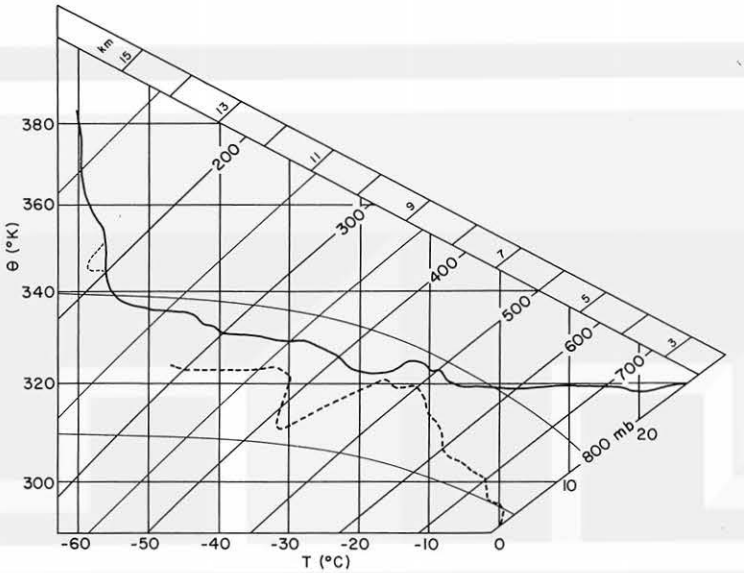

Fig. 1. The weighted-mean sounding from Flagstaff Airport for 1200 CST on 19 July 1960. Solid line - temperature. Heavy dashed line - dew-point temperature. Thin dashed line - cold bump on 1406 sounding.

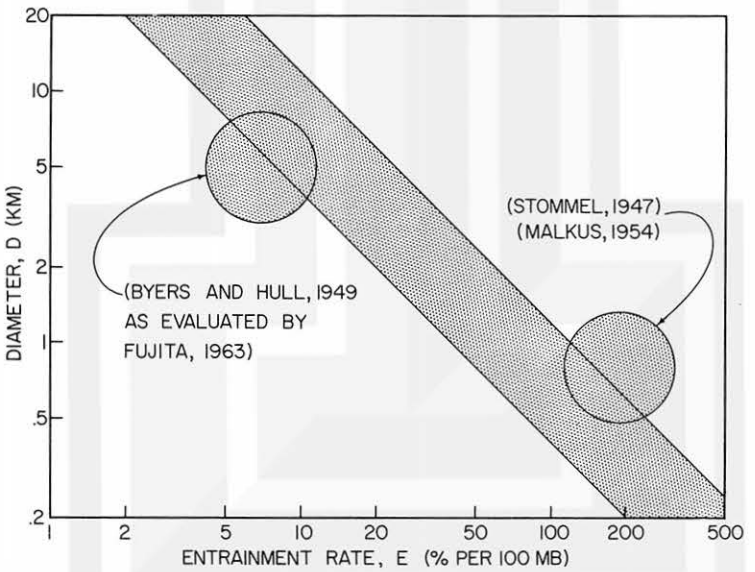

Fig. 2. Entrainment rate as a function of draft diameter. Slanting band represents range of values based on Eq. (13).

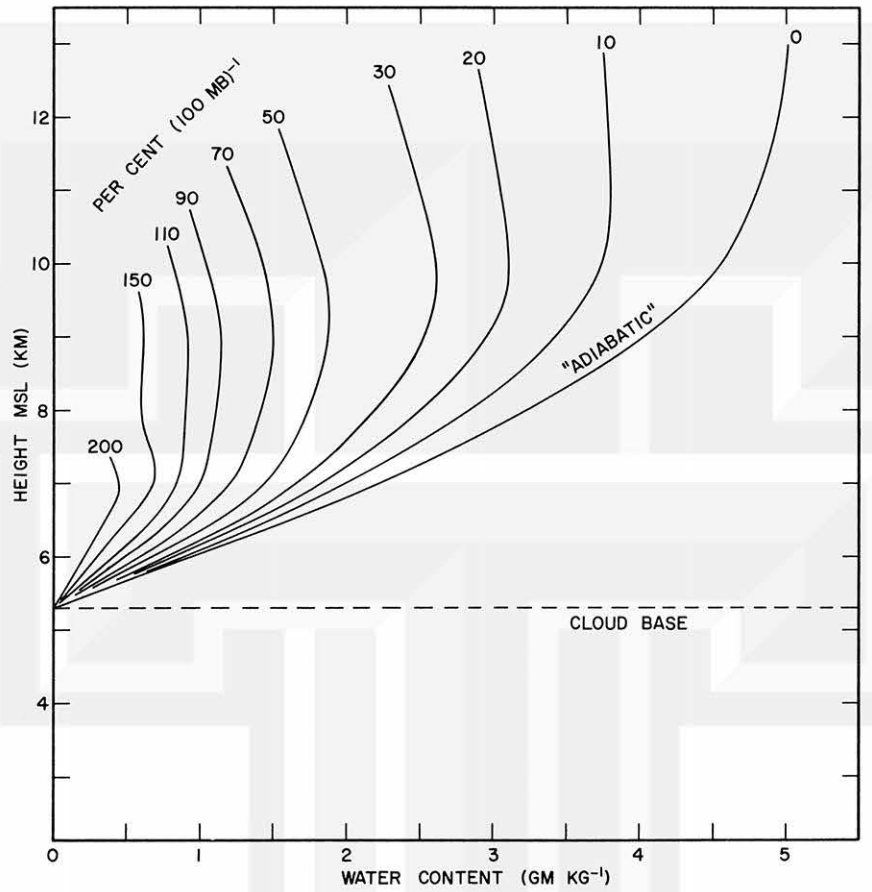

Fig. 3. Vertical distribution of mean water content as a function of entrainment rate.

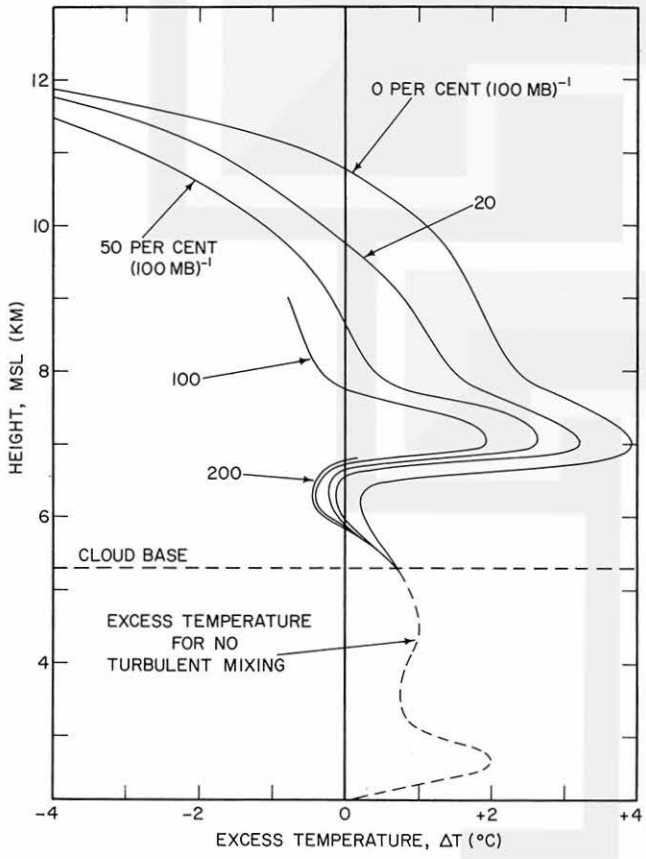

Fig. 4. Vertical distribution of temperature excess over that of the environment as a function of entrainment rate.

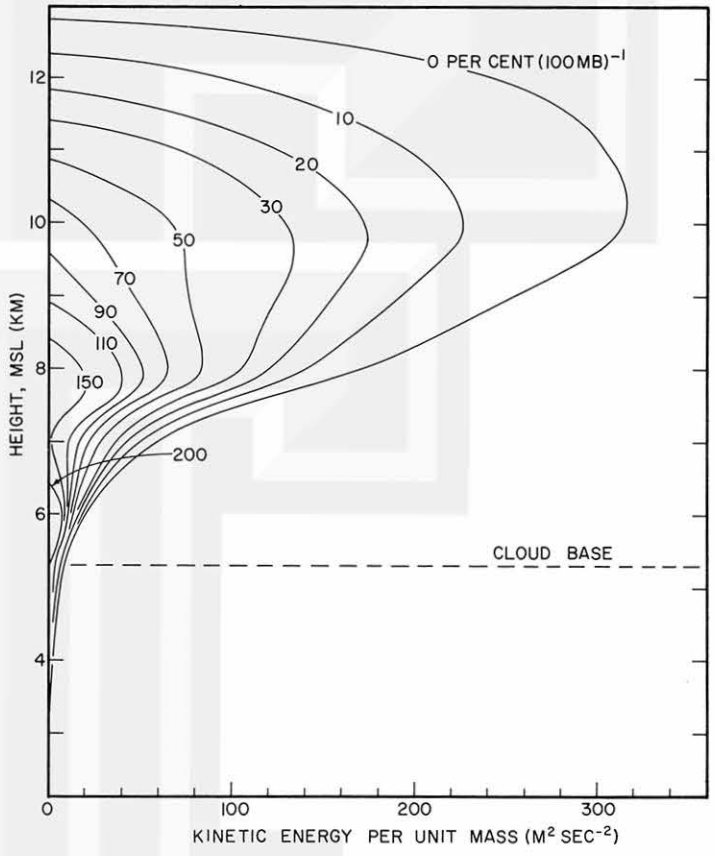

Fig. 5. Vertical distribution of kinetic energy per unit mass as a function of entrainment rate.

4. Environmental Conditions

For three successive summers (1959-61) Project Hi-Cue, a cloud physics research program, operated around the San Francisco Mountains (highest peak, 3.9 km) in northern Arizona; among the many participants were the University of Chicago, University of Michigan, Atmospheric Research Group, and Geophysics Research Directorate (now the Meteorology Laboratory of the Air Force Cambridge Research Laboratories). The mountainous area immediately north of Flagstaff forms a natural barrier to the moist southeasterly winds that pass over the Little Colorado Basin during the summer "monsoon" season. As a result, orographic activity is initiated which develops almost daily into hail-producing thunderstorms.

Fujita, Styber and Brown (1962) reported the favorable results obtained using their 1960 mesometeorological network to investigate orographic cumulus to cumulonimbus convection. Todd (1964) discussed the results obtained in studying cumulus development by combining time-lapse photographs and aircraft traverses. A photogrammetric study of the initial cumulus humilis activity on 19 July 1960 was made by Glass and Carlson (1963). Later the same morning there developed to the west of Flagstaff two cumulonimbi, of which the latter is being studied in this paper.

Figure 6 shows the region in which the cumulonimbus developed. The contour lines are drawn for 300-m intervals. All topography over 2.4 km above sea level is indicated by shading. It is noted that the three mountains and their cols form a barrier 2.5 to 3.9 km high (1.0 to 2.4 km above the Little Colorado Basin) to easterly winds that were prevalent on 19 July.

The plus signs in the figure represent the locations of the surface-wind equipment. Since the cumulonimbus developed outside the mesometeorological network, none of the other meteorological variables reflected the influence of the storm. The T-11 camera locations (A and B), as well as the outline of the area covered by this stereo-pair, are shown in the figure. The rawinsondes were released from Flagstaff Airport (camera site A).

Macrosynoptic situation of 19 July 1960. The synoptic weather patterns over the southwestern United States for 0500 MST on 19 July 1960 at the 700-, 500-, and 200-mb levels are depicted in Figs. 7, 8, and 9, respectively. It can be seen that at the 700-mb level (about 1 km above the ground) there was an easterly wind bringing moist air into the Flagstaff region. Since this wind was below the level of the cloud bases, the air was forced over the mountains leading to convective activity.

The 500-mb chart (Fig. 8) shows that much drier conditions existed above the

cloud base, a feature intensified by the northeasterly wind. The weighted-mean sounding (Fig. 1) shows a pronounced layer of drier air from 480 to 360 mb.

Conditions at the anvil level (200 mb) are found in Fig. 9; however, for a better idea of the 1200 MST winds at this level, consult Fig. 10 which shows the vertical profile of the horizontal wind for the Flagstaff releases at 0525 and 1406 MST and, for the 1100 pilot balloon release at Winslow, 87 km to the east. According to the Winslow release the edge of the anvil at 12.6 km would have to expand against a 5 m sec^{-1} easterly wind. This appears to be in conflict with the 1406 winds at the same level. However, as pointed out below, the balloon came within a few kilometers of the southeastern edge of the anvil, which could then explain the light, chaotic winds at this level.

Mesosynoptic situation. Figures 11 through 14 reveal the mesoscale conditions in the vicinity of the thunderstorm at 20-min intervals from 1120 to 1220 MST. The stippled areas are radar echoes for zero elevation (corrected for beam width) as obtained from the 22-cm Air Defense Command radar near Winslow. Thin lines represent cloud contours at 3-km intervals, the largest being the cloud base (5.3 km msl); in most cases only the base of the northernmost cloud mass could be seen in the photographs. This contouring was obtained by means of the simple triangulation of a given cloud element in the stereo-pair photographs. The two parallel lines denote the edge of the anvil; the procedure for determining the anvil outline is described in the next section.

The figures show that the clouds developed to the lee of the mountains, a characteristic feature of orographic clouds with bases higher than the mountain peaks. The air passing over Kendrick Mountain and the col between Kendrick and the San Francisco Mountains produced the two main cloudy areas. It should be noted that as the northwestern cloud moved to the southwest its rear edge remained over the lee slopes of Kendrick Mountain. The surface winds appear to have been under the influence of the topography until about 1220; by that time all of the stations began to show convergent flow toward the cumulonimbi.

In Fig. 11, the two radar echoes, which first appeared at 1117, were associated with the first cumulonimbus which reached anvil level some time after 1100. One notes that as this storm moved southwestward another one developed to the southeast of it; the new echo (associated with the cumulonimbus to be studied in detail) appeared aloft on the RHI scope at 1126 and on the PPI scope at 1132, just 3 min before the anvil began to spread out.

Movement of the first thunderstorm. Of the two echoes to appear at 1117, the one to the lower left moved from 035°; all other echoes shown in the sequence of figures moved from approximately 060°. This means that the largest echo, probably associated with the most active part of the first thunderstorm, not only moved to the left of the direction of motion of the other echoes but also to the left of any wind found in either the Flagstaff or Winslow releases.

It is known that large individual thunderstorms move to the right of the winds aloft (see, e.g., Byers, 1942; Hoecker, 1957; Fujita, 1958; Hamilton, 1958; Newton, 1960; Browning and Donaldson, 1963; Fujita, 1965). The authors are not aware of any accounts of storms moving to the left. However, such a movement can be explained in two different ways: a) If we accept Newton's (1960) hypothesis which treats of the winds relative to the cloud, then there is relative inflow at the lower levels from the southeast and relative outflow at the upper levels toward the southwest, resulting in an apparent movement to the left of the wind due to increased convective activity; or b) If we accept the idea of a rotating cloud producing the Magnus, or Kutta-Joukowski, effect as proposed by Byers (1942) and Fujita (1965), then a cloud rotating anti-cyclonically would move to the left of the wind. It is not possible to say which, if either, of these theories actually explains the echo's movement; no measurements were made near the cloud and the only photographic evidence of its existence is seen in the background of Fig. 24. A more detailed study of this situation will be reported elsewhere.

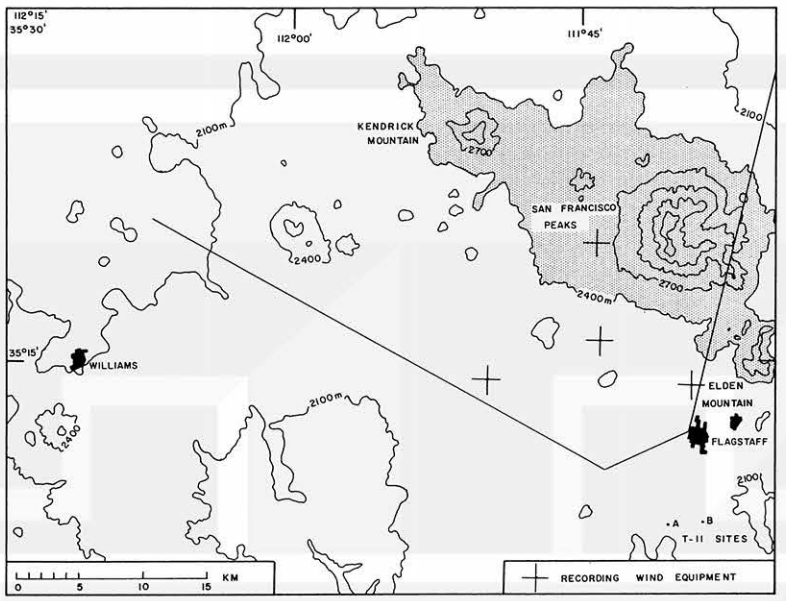

Fig. 6. Base map of area of orographic activity. Stereo T-11 camera sites are A and B, with region of coverage indicated. Contours are for intervals of 300 m.

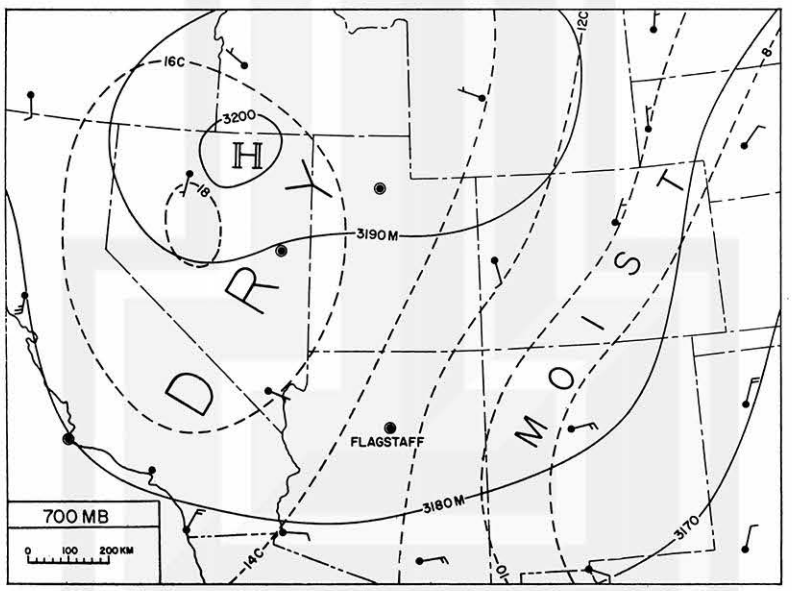

Fig. 7. 700-mb chart for 0500 MST on 19 July 1960. Solid lines are height contours (meters). Dashed lines are isotherms (^{o}C). Long wind barb is 5 m sec^{-1}.

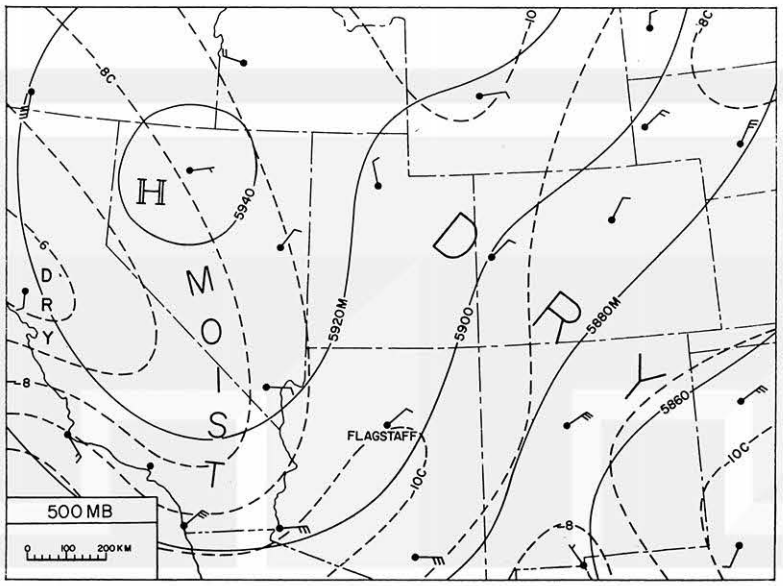

Fig. 8. 500-mb chart for 0500 MST on 19 July 1960. Solid lines are height contours (meters). Dashed lines are isotherms (^{o}C). Long wind barb is 5 m sec^{-1}.

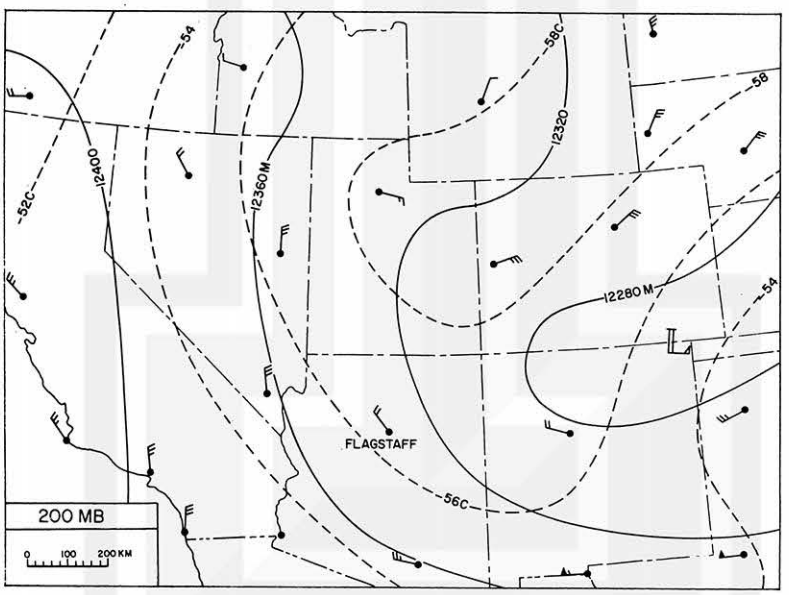

Fig. 9. 200-mb chart for 0500 MST on 19 July 1960. Solid lines are height contours (meters). Dashed lines are isotherms (^{o}C). Long wind barb is 5 m sec^{-1}.

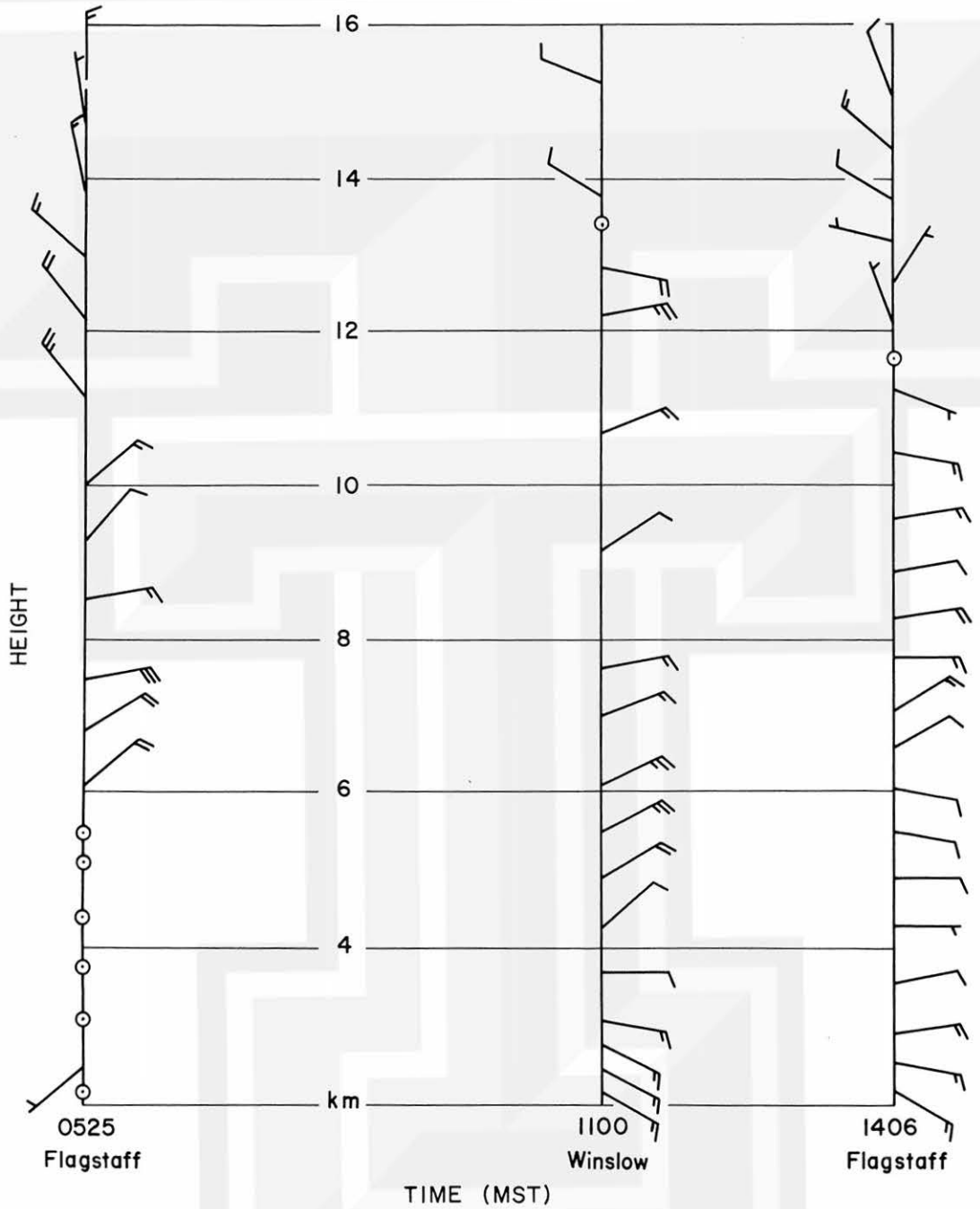

Fig. 10. Vertical distribution of the horizontal wind at Flagstaff and Winslow on 19 July 1960. Long wind barb is 5 m sec^{-1}.

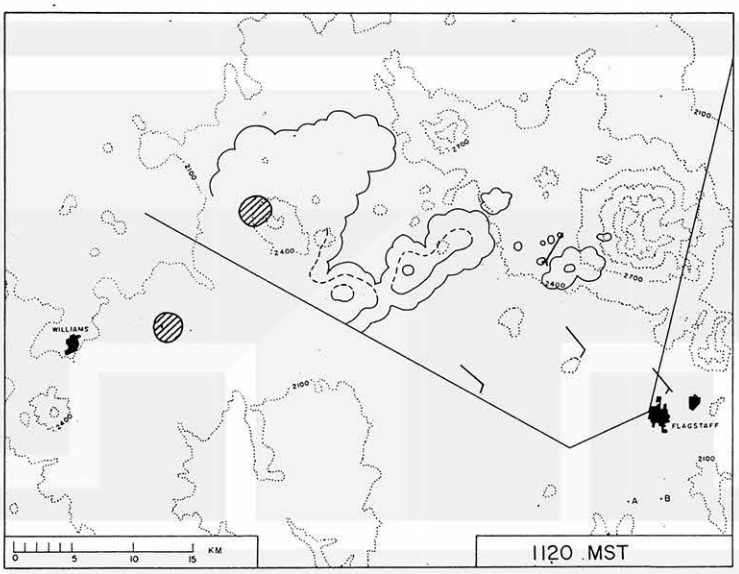

Fig. 11. Cloud distribution and surface winds at 1120 MST. Long wind barb is 5 m sec^{-1}. Forked tail in place of barb indicates missing wind speed. Cloud contours are at 3-km intervals above cloud base (5.3 km, msl). Shading indicates radar echoes. Base map is the same as in Fig. 6.

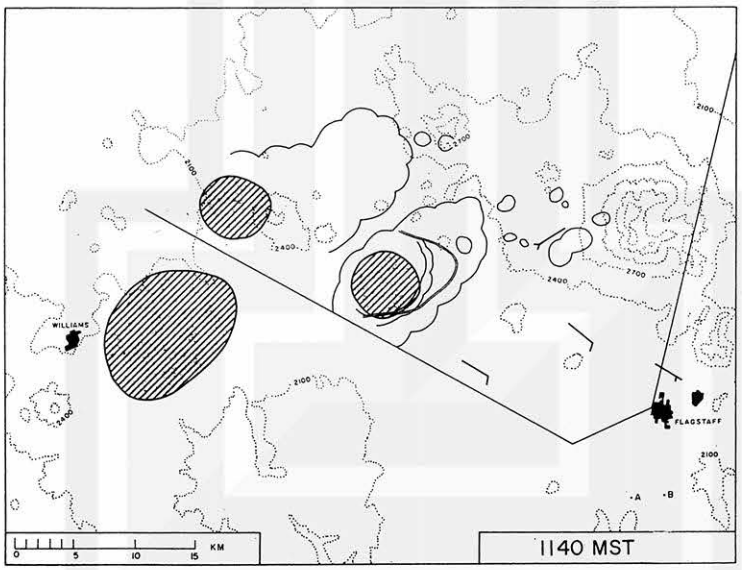

Fig. 12. Same as Fig. 11, but for 1140 MST. Two parallel lines indicate the outline of the anvil's edge.

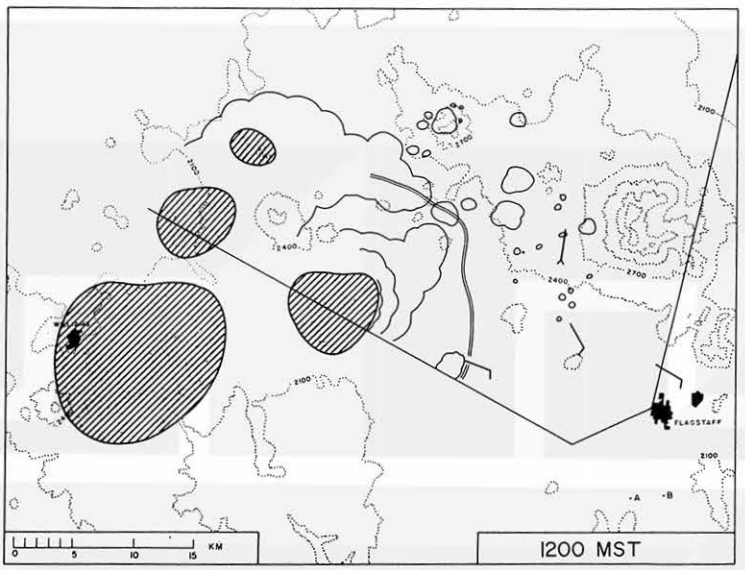

Fig. 13. Same as Fig. 12, but for 1200 MST.

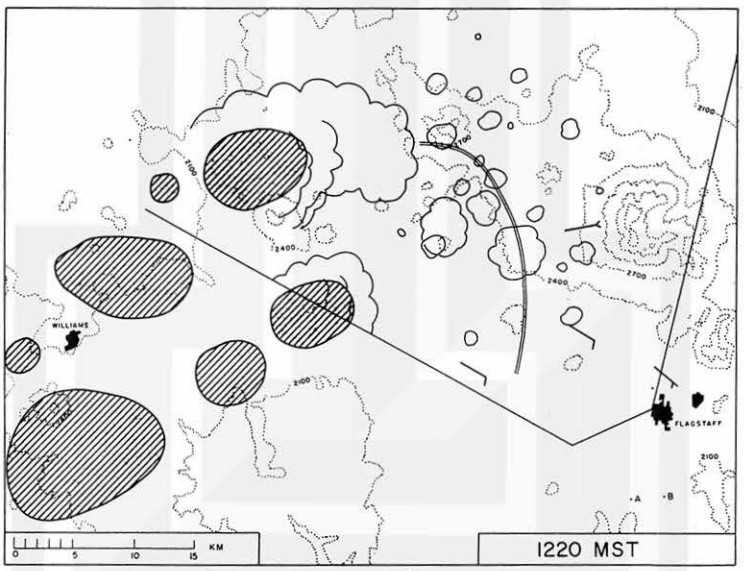

Fig. 14. Same as Fig. 12, but for 1220 MST.

5. Photogrammetric Analysis of the Cumulonimbus[1]

Photogrammetric reduction procedure. Since the pair of cameras used in this study were not oriented perpendicular to the baseline, contrary to the situation in the case of Glass and Carlson (1963), it has been necessary to expand upon their procedure; however, for a detailed description of the computer programming used in this reduction process, refer to Schurz and Perssen (1964).

The reconstruction of the position of an identifiable cloud point in space as it changes with time is accomplished by the following sequence of steps: a) location of the cameras in a suitable coordinate system, such as the State Plane Coordinates, and orientation of both cameras with respect to the coordinate system; b) measurement of the x and z photo coordinates, parallaxes of cloud points, and the focal lengths of the reference photograph during the time the cloud point is under study; and c) conversion of the adjusted photo coordinates to suitable space coordinates.

The requirements of a) are satisfied by carefully surveying the two camera sites - choosing from each site up to six control points across the camera's field of view and then determining the azimuth and elevation angles of the selected objects. The surveying instrument (Wilde T-2) permits measurements to 1 sec of arc; therefore, the limiting precision is determined by the nature of the control points chosen. For example, a sharp mountain peak may be quite rounded when viewed through the theodolite; on the other hand, a well-defined point such as a fire tower may not be visible on the photograph.

The tilt of a camera, i. e., it's ω rotation about the x-axis, is found by computing a line of best fit to the differences (Δz's) between the measured (z_m) and computed (z_c) photographic plate coordinates of the control points:

$$\Delta z = z_m - z_c$$

and

$$z_c = \frac{F_z \tan V}{\cos\left[\tan^{-1}(x_m / F_x)\right]},$$

where F_z and F_x are the respective focal lengths in the z- and x- direction, V is the surveyed vertical angle of control point, and x_m is the measured plate coordinate in x-direction. With the predicted value of $\Delta z'$ from the line of best fit evaluated at x=0 one obtains

$$\omega = \tan^{-1} \frac{\Delta z'}{F_z}.$$

---

[1]Morton Glass of the Air Force Cambridge Research Laboratories kindly provided the general information and data obtained from the precise reduction procedure that are presented in the first three sub-sections and the unpublished findings presented in the second sub-section.

The swing, k, i.e., the rotation of the camera about its y-axis, is given by $k = \tan^{-1} S$ where S is the slope of the line of best fit discussed above. The tip, (α), of a camera is its rotation around the z-axis and is computed relative to an east-west line, i.e., the x-axis of the State Plane coordinate system.

The horizontal calibration is obtained as follows: an x-coordinate, x_c, of a control point is computed in the coordinate system of the camera from $x_c = F_x \tan(\theta)$, where θ is its surveyed horizontal azimuth minus the camera's grid aximuth ($\psi+\phi$). The measured coordinate, x_m, adjusted for the effects of swing, tilt, and lens calibration is given by $x_m = F_x \tan \beta$.

The amount of tip, ΔH, for a control point is then obtained from

$$\tan \Delta H = \tan(\theta - \beta).$$

The tip for a given photograph is the average of all the control points plus the camera's grid azimuth,

$$\alpha = \overline{\Delta H} + (\psi + \phi).$$

The tip, tilt, and swing are determined for each camera on a sufficiently representative number of photographs over the period of observation; they are then averaged and applied to the computation of space coordinates of cloud points from the stereo photographs.

Prior to measurement (step b) a careful survey of the entire sequence of stereophoto pairs of the cloud being studied is made both to select the cloud points which adequately define the cloud characteristics and to determine their suitability for measurement. This includes viewing in stereo each of the photo pairs to assure that points chosen are available for parallax measurement. Cloud points usually can be followed for 3 to 8 minutes until mixing with the environment causes their erosion.

The raw plate coordinates x_i and z_i ($i = 1 \ldots m$) of the series of cloud points, as taken from the reference photograph (in this study photographs from site A), are adjusted for shrinkage and scaled to a nominal focal length

$$x_i Q = x_i \frac{F_x Q}{F_{x_i}},$$

where F_{x_i} is the focal length in the x-direction measured at the same time as x_i and $F_x Q$ is a nominal focal length; the coordinate z is handled similarly. An alternative to measuring the plate coordinates at each point of the series is available. This second procedure, which is preferred, sums the movement of the points in the series

in order to compare them with initial and final plate coordinates. An adjustment factor is determined which permits a check on the consistency of the data and provides a means for smoothing the series.

The absolute parallax of the point is obtained with the use of a Zeiss Stereotope; it is the sum of the observed depth parallax and a reference parallax. The reference parallax is found with the use of scored fiducial lines, reference points in space, or with grids mounted on the Stereotope.

The computed parallax, P, is used with the adjusted x-coordinate of the point in the reference photo ($x Q_i$) to find the x-coordinate in the auxiliary photo. Since

$$P = xQ_i - x_i ,$$

x_i is obtained. The final adjusted auxiliary coordinate is now computed,

$$x Q'_i = x'_i \frac{F_x Q}{F_{x_i}} ,$$

where the prime refers to a measurement on the auxiliary photograph (from site B).

The x, y, z photo coordinates ($y = f_x$, f_x being the focal length) from the reference camera and information to determine a scale factor are now available for conversion to space coordinates, the final step in the data reduction procedure. This is accomplished by a 3 x 3 matrix rotation of the reference photo coordinates through $(\alpha'-\alpha), \omega, k$ into the auxiliary coordinate system defined by the auxiliary photo coordinates.

A set of intersection coordinates (X_A Y_A Z_A) parallel to the auxiliary camera but with origin at the reference camera is defined. With reference to Fig. 15,

$$\frac{Y_A}{f} = \frac{AE}{P} = \frac{AD + DE}{P} ,$$

where $P = x_A - x_B$ is the parallax and Y_A is the Y range from the reference camera averted ψ degrees with respect to the camera coordinate system. But it is seen that

$$AD = \overline{AB} \cos\psi$$

and

$$DE = x_B \frac{\overline{AB} \sin\psi}{f}$$

where $\overline{AB}$ is the baseline between the two cameras. Therefore

$$Y_A = \frac{f\ \overline{AB} \cos\psi + x_B\ \overline{AB} \sin\psi}{P}$$

or

$$Y_A = \overline{AB} \left(\frac{f - x_B \tan\alpha}{P} \right) \cos\alpha , \qquad (14)$$

where $\alpha = (\psi + \phi)$ is the avertance of the cameras from the State Plane coordinate system (X, Y) assuming that the deviation $\overline{\Delta H}$ is zero. Similarly, once Y_A is known, it is seen from Fig. 15 that

$$X_A = x_A \frac{Y_A}{f} \qquad (15)$$

and

$$Z_A = z_A \frac{Y_A}{f} . \qquad (16)$$

By rotating X_A, Y_A, and Z_A through $-\alpha'$, $-\omega'$, $-k'$ and translating the origin, the set of State Plane coordinates of each cloud point is determined.

Successive pulsations developing into the cumulonimbus. From a systematic photogrammetric analysis of emerging cloud thermals, it was possible to obtain a quantitative description of the development of the cumulus congestus cloud from its early stages to the onset of anvil formation. Measurement of the anvil development and outflow is described in the next sub-section.

The congestus cloud growth is characterized by successive pulsations of cloudy material, each forming upwind of the preceeding cloud mass, and each originating at essentially the same point in space as the preceeding. Figures 16 and 17 are a series of T-11 photos of the growth history of the cloud studied. The numbers refer to representative cloud points whose position with time was measured. When paired photos are viewed in stereo, at least four major pulsations could be discerned and followed well after they had merged with the main cloud mass. The cloud points representing the earliest positions of each of the four cloud masses were found to have a total spread in the horizontal of less than 0.8 km. The process of development by successive pulsations can be seen by following the three individual masses, marked A, B, and C, that were studied throughout their growth.

It appears likely that the upwind topography is the source of buoyant air and that continued development of the cloud required that it remain relatively fixed with respect to its source. In addition these pulsations had to be sufficiently buoyant and occur with sufficient frequency to contribute to the ultimate development of the cumulus congestus to an organized thunderstorm.

Evidence of the growing organization of the cumulus congestus cloud was found from an analysis of the growth history of each of the cloud mass pulsations. Penetration of the individual cloud mass to its maximum height as well as its increase in volume was accomplished by successive penetrations of cloud thermals. Representative

diameters of each of the group of cloud thermals comprising a cloud mass were found to increase with height and the maximum vertical velocity of the thermal cap to increase with diameter. Figure 18 shows this relationship for thermals comprising three cloud mass pulsations. In addition this figure indicates a tendency towards larger values of vertical cap velocities, for a given diameter, occurring with the later pulsations. (It should be mentioned that while the largest values (~ 8 m sec^{-1}) of vertical velocity were measured in Group C, they occurred just prior to penetration of a stable layer at approximately 12.5 km and are not shown here since with the initial anvil formation a diameter measurement consistent with previous measurements could not be made).

This indication of the growing organization of the cloud is more clearly shown in Figs. 19 and 20. These figures give the history of two cloud mass pulsations; Group A being the earliest, Group C the last. The broad shaded lines indicate the average position (and time) of the group of "cloud thermals" comprising the pulsation. A series of tracing of the time lapse photos of the last "thermal" in the group is shown in the upper right hand corner. The following features should be noted: The height to which Group C builds is greater than A; the maximum vertical growth rate of Group C occurs at a higher elevation, and its magnitude during the period of most rapid growth is also greater than Group A. A sequential change in the parameters mentioned above consistent with Groups A and C was observed from data of Group B and a fourth partially analyzed group, the latter two occurring between A and C.

The suggested mechanism for the growing intensity of succeeding cloud mass groups is entrainment of moist air from preceding cloud elements. Succeeding cloud groups being less modified by the environment contribute to the growing volume of the cloud system. Development to the thunderstorm stage would then be the result of an increasingly protected core of vertical drafts.

Photogrammetric technique for mapping the expanding anvil top. Using the precise reduction procedure outlined at the beginning of this section, x, y, z measurements of about 350 points along the visible edge of the anvil (eastern portion) were made from 1138 to 1216 MST. After plotting the data points on a horizontal plane, smoothed isopleths of height were drawn. From this a variable-height height grid (Fig. 21) was constructed by making use of elementary trigonometry. As the thunderstorm moved westward, the rear of the anvil expanded continuously eastward relative to the ground; this made it possible to accurately draw the horizontal projection of the

visible anvil at a given time by using just one of the stereo-pair photographs.

This simpler, yet somewhat less precise, photogrammetric technique allows the direct transfer of the anvil outline from the photograph to a horizontal base map - a procedure which involves a tilt grid (Fig. 22) placed on the photograph and the height grid (Fig. 21) that has been constructed to the scale of the base map. Since the cameras were facing horizontally (tilt angle of 90^{o} from the nadir), the tilt grid consists simply of two sets of parallel lines. In both Figs. 21 and 22 the lines going from top to bottom are the intersections of the two grids by vertical planes one degree apart radiating out from the camera. The one plane that passes through the camera's optical axis is called the principal plane and its intersection with a grid is called the principal line. The horizontal lines are the intersections of the two grids by planes one degree apart radiating out from a common horizontal axis, which passes through the camera and is perpendicular to the principal plane.

As an example of how the two grids were used, Figs. 21 and 22 contain a tracing of the anvil at 1150. It can be seen that for points at the same height, those highest in the photograph are closest to the camera. Therefore, in transposing the outlines from the tilt grid to the height grid, there is a direct relationship when the height grid (on translucent paper) is flipped over, so that the principal line remains on the right and the radial lines converge toward the top of the grid.

Using this procedure, the anvil outlines were drawn at two-minute intervals from 1138 to 1216. In order to follow individual features along the edge of the expanding anvil, a composite photograph was constructed (Fig. 23). The only known picture of the entire cumulonimbus after the anvil was well-developed is presented in Fig. 24 which was taken at 1150 from a point in the eastern part of Flagstaff.

Figure 25 shows the anvil outlines after they were adjusted relative to the center of the cumulonimbus by subtracting the translational speed (3.2 m sec^{-1} from 060^{o}) as determined from the mean speed of the radar echo during the period of study. Connected dots show the successive positions of individual anvil elements; they were determined by carefully studying the composite photograph (Fig. 23). Spacing of the outlines reveals a general increase in the expansion rate with time which ranges from 5 to 10 m sec^{-1} relative to the center of the cloud. The trend toward increased outflow suggests that the updraft became more organized, and perhaps more widespread, after the spreading anvil provided an exhaust for the upward-moving air.

Flux of air into the anvil. The photographic evidence, especially Fig. 24, indicated that the cumulonimbus was rather symmetric, as one might expect from the

relatively light and uniform winds aloft indicated in Fig. 10. This feature was used to advantage in the computation of the mass flux into the anvil.

In the bottom half of Fig. 26 the approximate outlines of the stem and anvil of the cloud are depicted; the top of the anvil was drawn flat in order to simplify the calculations. The shape of the anvil outlines was determined from the series of time-lapse stereo-pair photographs (see Fig. 23). Since the entire diameter of the cloud was not shown in the later photographs, both the 1150 photograph (Fig. 24) and the position of the center of the radar echoes were used in conjunction with the stereo photographs to provide the radius information found in Fig. 26a.

From a symmetric loud, the mass, M, in the anvil at any given time can be determined from

$$M = 2\pi\bar{\rho}\int_0^R r\,\Delta h\,dr, \qquad (17)$$

where $\bar{\rho}$ is the mean density in the anvil, R is the radius of the edge of the anvil, and Δh is the variable thickness of the anvil. As seen in Fig. 26a, the mass in the upper part of the stem has been included with the mass of the anvil itself; since the cloud stem is fairly straight from the level of maximum vertical velocity (roughly 10.3 km) to the bottom of the anvil, almost all of the air that ascended through the level of maximum vertical velocity passed into the anvil. This feature is needed later in order to compute the vertical velocity in the cloud.

In Eq. (17), Δh is a function of radius; therefore, as a means of evaluating the integral graphically, $r\,\Delta\,h$ was plotted as a function of r in Fig. 26b. A planimeter was used to compute the mass in the upper stem and anvil at five-minute intervals. As a point of interest it may be noted in Fig. 26b that, except for the first 10 min, the depth of the stem arbitrarily included in the calculations makes a negligible contribution to the mass in the anvil itself.

The mass flux into the anvil was determined from the increase in the mass, M, during each of the five-minute intervals. The resulting flux is indicated by the lowest curve (0 per cent) in Fig. 27. This curve represents the flux, if it is assumed that no air passed through the visible edge of the anvil. The other five curves indicate the flux if 10, 20, 30, 40, and 50 per cent of the mass that entered the anvil from below passed out through the visible part of the anvil; it is not possible to say from the data which curve is most appropriate. However, the figure does indicate that the vertical flux in the upper part of a moderately-sized thunderstorm is of the order of 10^8 kg sec^{-1}. Based on Thunderstorm Project data, Braham (1952) found that the

vertical mass flux in cumulus congestus and small cumulonimbus clouds was of the order of 10^7 kg sec^{-1} ; this agrees with the flux values just after the anvil formed (Fig. 27). In cumulus clouds studied by Anderson (1960), the flux was found to range from 10^5 to 10^6 kg sec^{-1} in small cumuli to 10^7 , and even 10^8, kg sec^{-1} in cumuli congesti. As a consequence Anderson speculated that the flux may exceed 10^9 kg sec^{-1} in well-developed thunderstorms.

In connection with the family of curves in Fig. 27, it might be well to cite the evidence that exists in this case for the air in the anvil expanding at a faster rate than the visible part of the anvil; i.e., evidence that air passes through the sides of the anvil. First of all, in spite of the long-lived features along the edge of the anvil (Figs. 23 and 25), the fact that there were minor changes indicates that the ice crystals at the sides of the anvil should be sublimating, especially due to small-scale turbulence.

An additional piece of evidence is the cold bump in the sounding (Fig. 1) just above the 200-mb level. The coldest part of the bump occurs at the level of the leading edge of the anvil. Although the exact location of the leading edge at that time is not certain because the portion closest to the balloon at that level was southwest of the cameras' coverage area, a rectification of the available data indicated that the balloon was 5 to 10 km from the visible anvil. Therefore, air had to be flowing through the anvil.

Most convincing evidence is presented in Figs. 28 and 29. From 1143 until 1222, a B-47 aircraft (dashed path) flew around the region indicated in the figures. The dashed rectangle is the area contained in Figs. 11-14; the dotted outline represents the approximate extent of the major cloudiness. The temperatures[2] measured by the aircraft were adjusted to a common level (11.3 km) by using the mean sounding's lapse rate. The temperature analysis was broken up into two parts - one for each pass near the clouds. Both figures show that the axis of warmer temperatures is oriented in the direction of the wind (see Winslow winds in Fig. 10) and that the warmest values occur downwind from the clouds.

---

[2]A study of the vortex temperature measurements indicated that they averaged 3C higher than the 1406 rawinsonde. It was further revealed that the measurements were 0.16C higher during turns than during straight segments of flight. Therefore these corrections were taken into account before the data were analyzed.

It seems reasonable and most obvious that the warming is due to dry-adiabatic compression of outflow air descending 1.3 km from the anvil. This explanation should require a) that the warmest temperatures be associated with and downwind of a cumulonimbus, having drifted away from that cloud as it descended and b) that the warming become more intense and widespread as long as there is an actively growing cumulonimbus present in the warmest region. Since both of these requirements are fulfilled, it is assumed that the warming is direct evidence than an appreciable amount of the flux into the anvil passes through the visible edge.

Photogrammetric evidence for rotating thunderstorms. It is known that the severe thunderstorms with which tornadoes are associated rotate cyclonically (see, e.g., Fujita, 1960). In his model of severe local storms, Browning (1964) proposed that the updraft spirals cyclonically upward. The authors knew of no visual evidence indicating that non-tornadic thunderstorms or cumulus congestus rotate, so they decided to use the anvil measurements shown in Fig. 25 to ascertain if the cumulonimbus rotated.

The lines connecting the dots in Fig. 25 were extended backward toward the center of the cloud; the center of the partial envelope formed by the extensions was taken as the center of the cloud. Based on the dot-connected curves, a more complete family of streamlines was drawn; then an isotach pattern was made from the movement of points along the anvil's edge. By dividing the anvil into 10^{o} arcs and approximating the edge within each arc by a segment of a circle, the vorticity could be calculated from the simplified expression,

$$\zeta_a = \frac{4v_t}{D} + f , \tag{18}$$

where ζ_a is the absolute vorticity, v_t is the tangential velocity, and f is the Coriolis parameter. A mean value of the vorticity along the entire edge was computed for each 2-min interval.

Figure 30 shows the mean vorticity as a function of the mean diameter of the anvil; the dashed parts of the curve indicate that the mean was based on only 8 or 9 values. It is evident from the figure that the anvil rotated cyclonically and that its rate of rotation decreased as the anvil became larger; this latter effect is due mostly to the decrease in vorticity with increasing diameter in (18), but there is an additional slow-down due to viscous effects which is exhibited by the change to negative curvature. It should be remembered that the figure shows the vorticity along the edge of the anvil.

If the vorticity of the anvil is initially as high as 10^{-3} sec^{-1} or even 10^{-2} sec^{-1}, one might expect the rotation to be quite evident. However, this is not the case because an anvil 6 km in diameter would completely rotate once in one hour. By the time the anvil becomes 15 km in diameter, it would take 5 hr to make one rotation. One would find it extremely difficult to detect the rotation of even a newly formed anvil because of the combined motions involved in a rotating and expanding anvil that is attached to a translating cloud. Therefore, it is quite possible that nearly all cumulonimbi do rotate but that they escape detection by ordinary means. It is understood, of course, that a cyclonically rotating anvil is merely a consequence of the rotation experienced by the ascending air in the stem of the cloud; the air inside the cloud would be rotating considerably faster than the air in the expanding anvil.

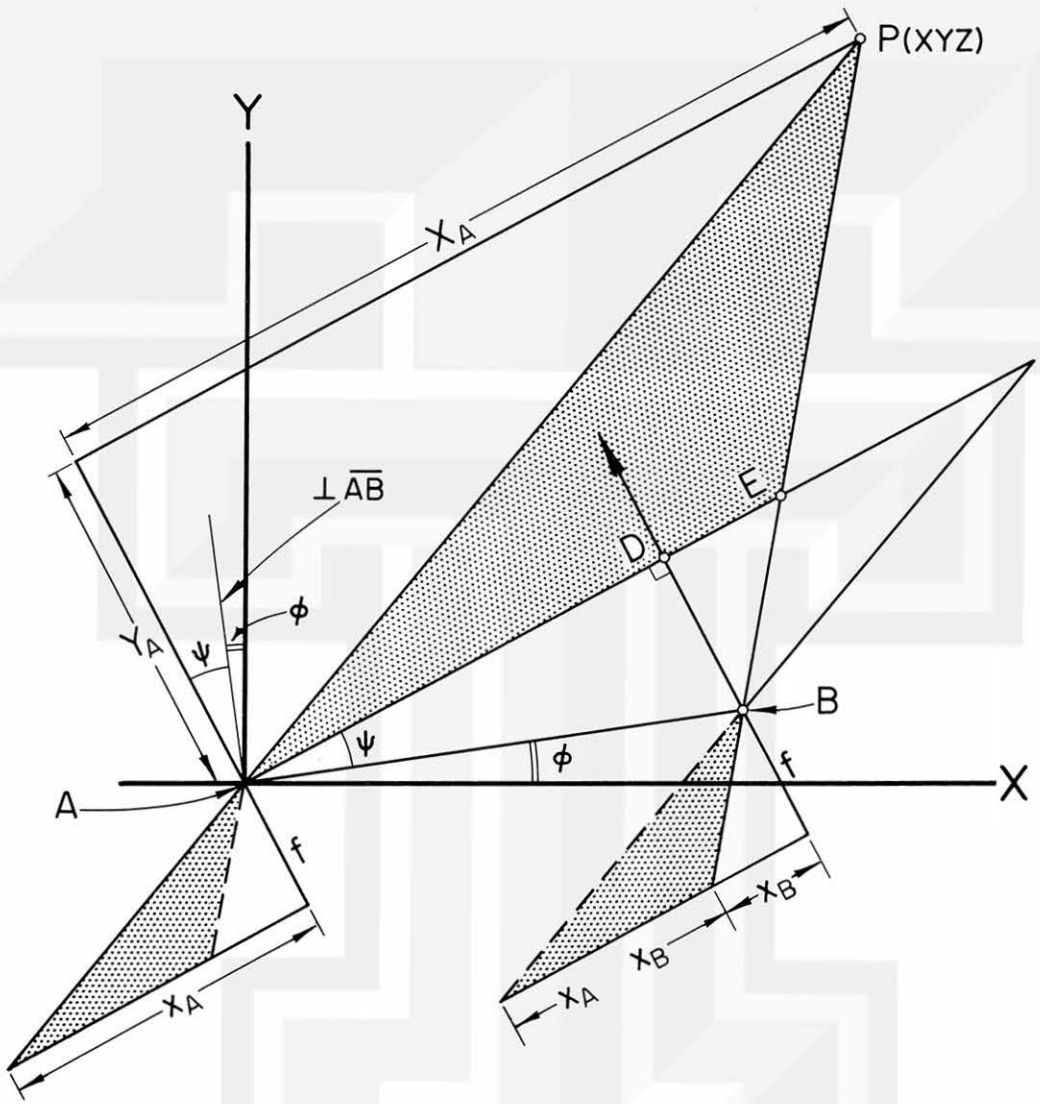

Fig. 15. Geometry for triangulation of point P(XYZ) from camera sites A and B. See text for explanation.

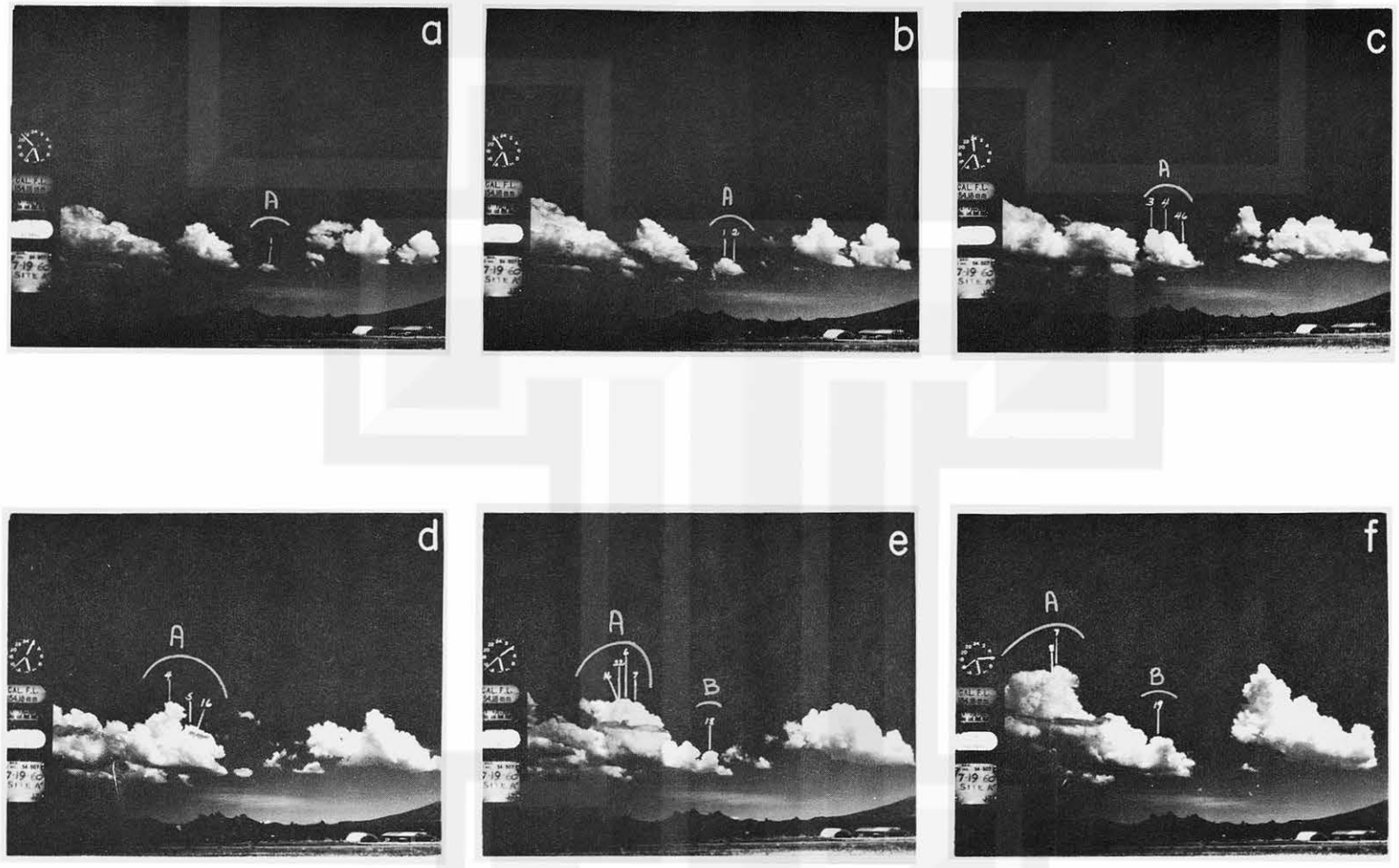

Fig. 16. Cumulus cloud growths as seen from Site A at a) 1053, b) 1055, c) 1100, d) 1105, e) 1110, and f) 1115 MST. Numbers refer to cloud elements that were followed with time. Courtesy of M. Glass.

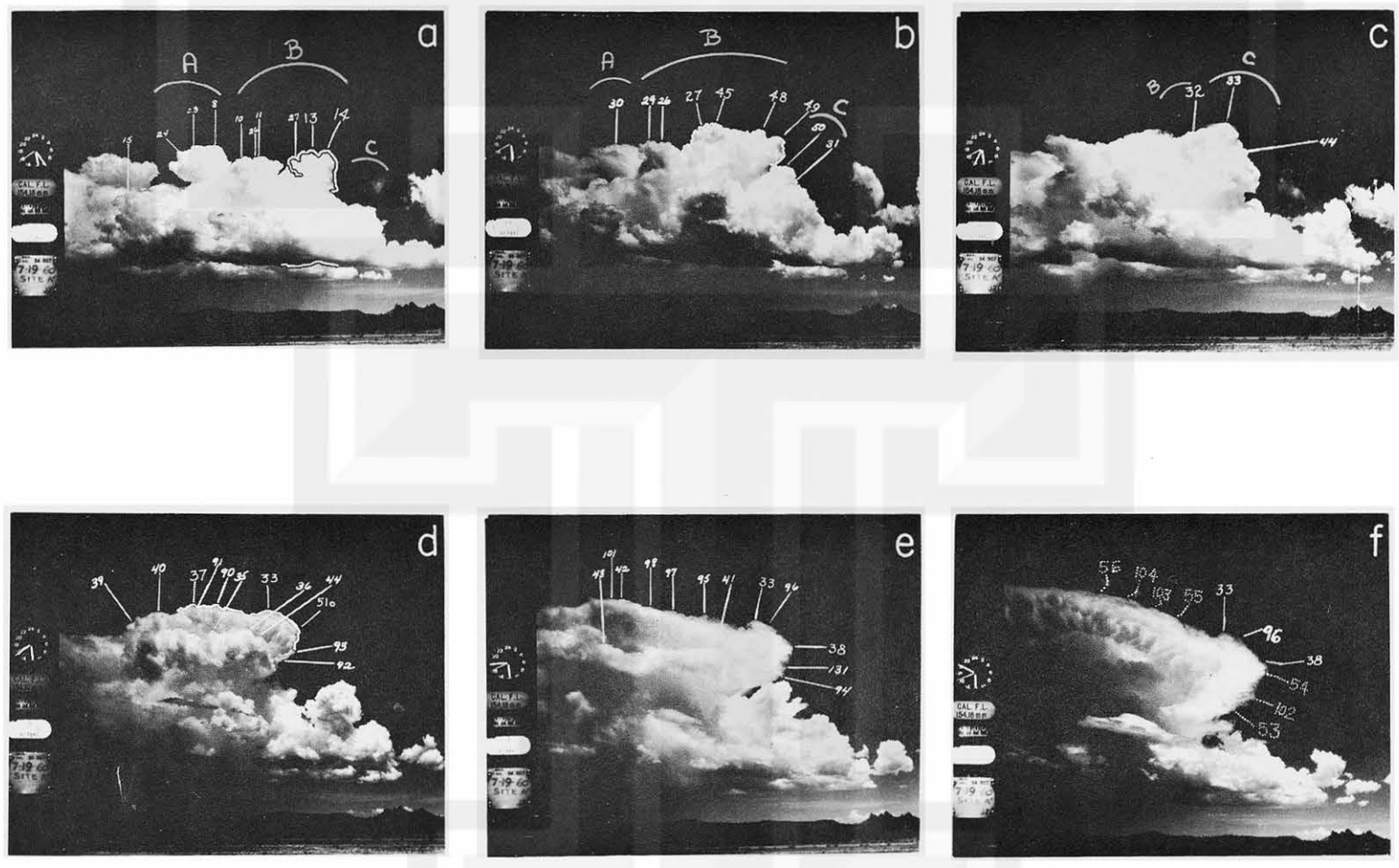

Fig. 17. Cumulus congestus to cumulonimbus growths as seen from Site A at a) 1125, b) 1130, c) 1135, d) 1140, e) 1145, and f) 1150 MST. Numbers refer to some of the cloud elements that were followed with time. Note that orientation of camera has been changed from that used in Fig. 16. Courtesy of M. Glass.

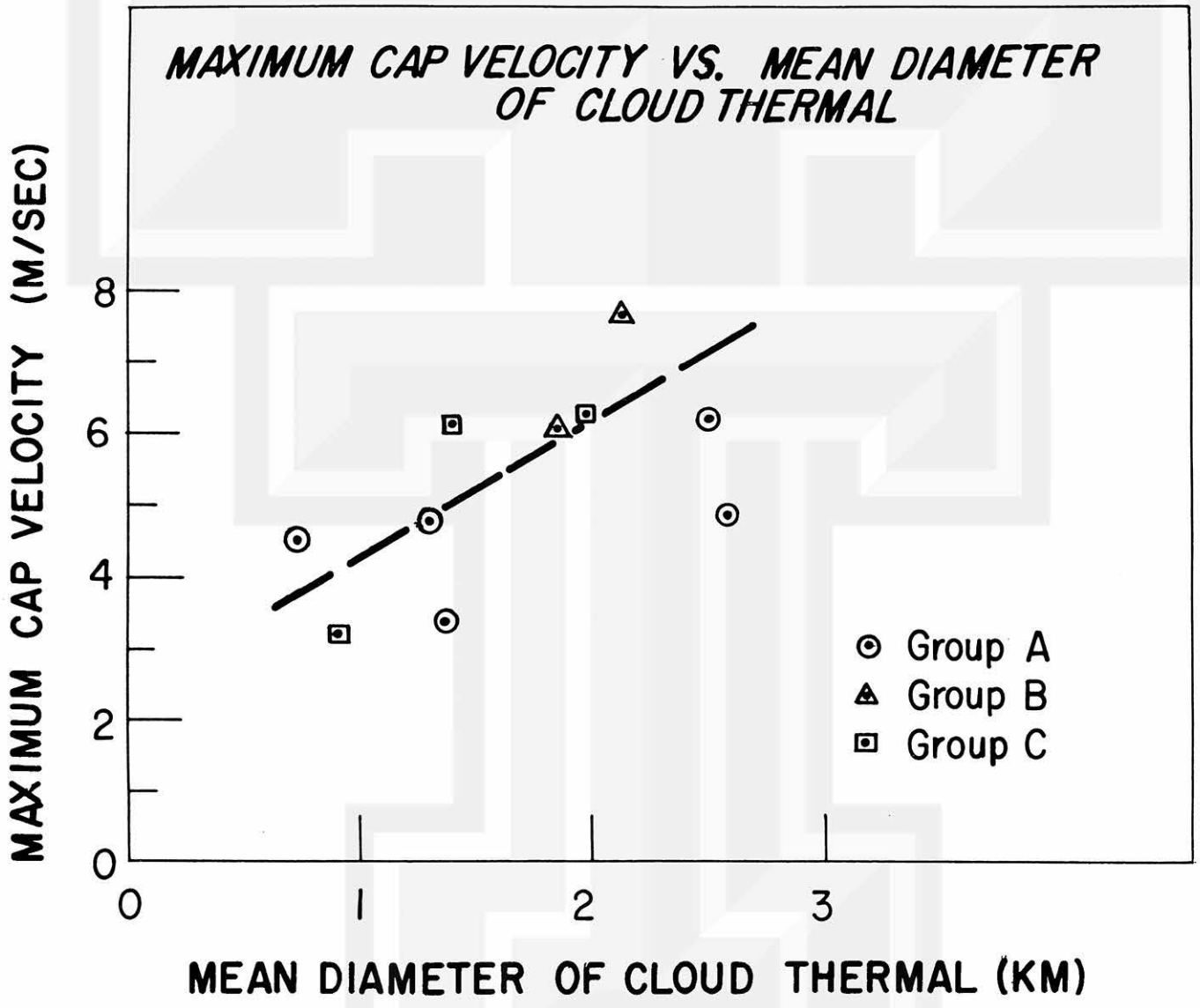

Fig. 18. Maximum cap velocity as a function of mean diameter for Groups A, B, and C. Courtesy of M. Glass.

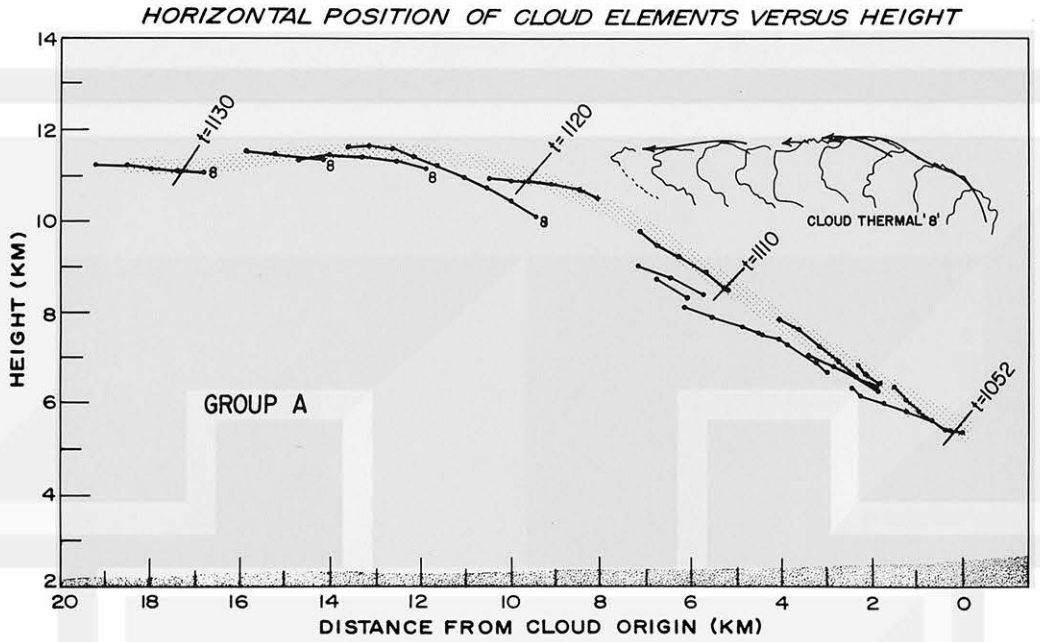

Fig. 19. Vertical growth of Group A. Insert shows one-minute outlines of cloud thermal 8, which was the last one of the group. Courtesy of M. Glass.

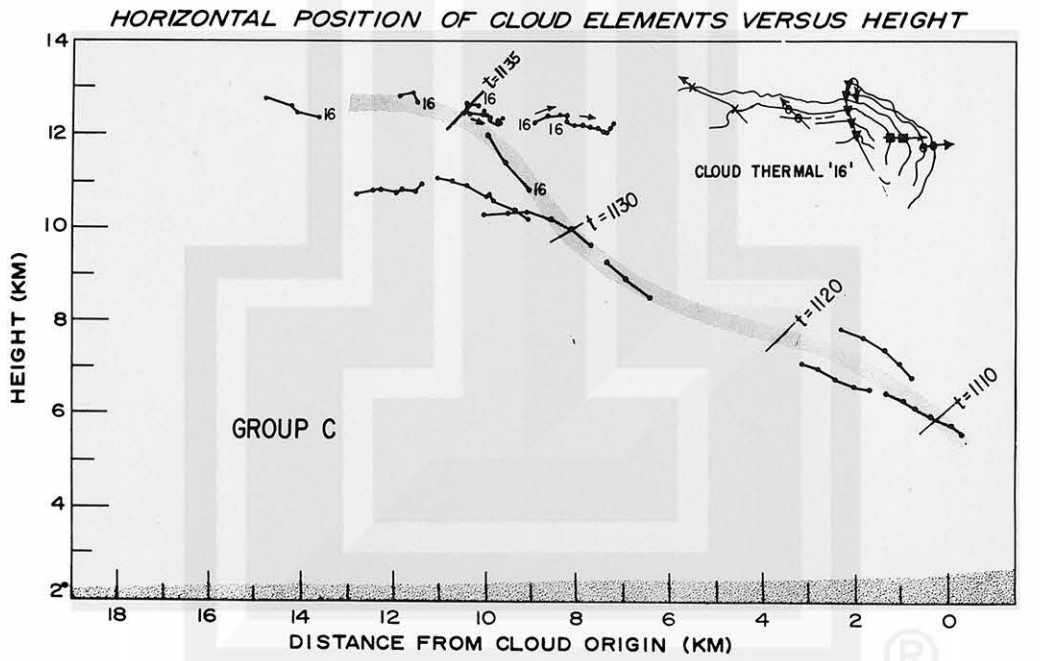

Fig. 20. Vertical growth of Group C. Insert shows one-minute outlines of cloud thermal 16, which was the last one of the group. Courtesy of M. Glass.

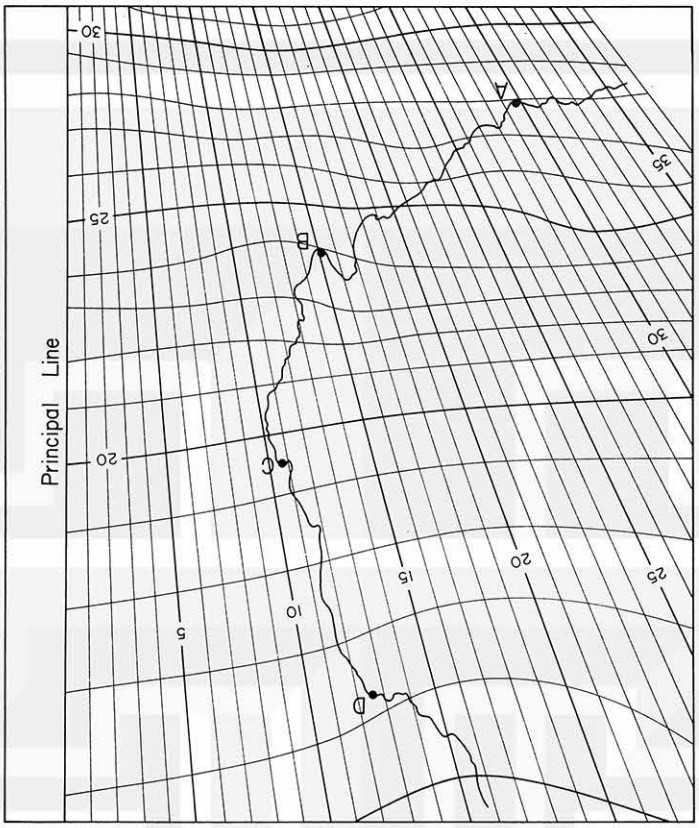

Fig. 21. Variable-height height grid with outline of anvil at 1150. See text and Fig. 22 for use of grid.

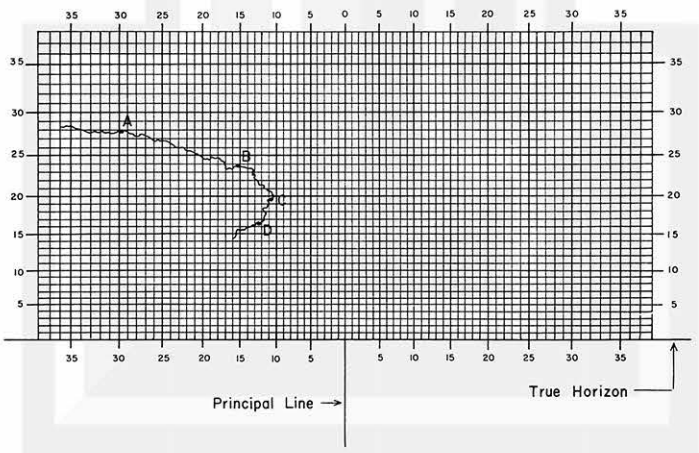

Fig. 22. Tilt grid with outline of anvil at 1150. See text and Fig. 21 for use of grid.

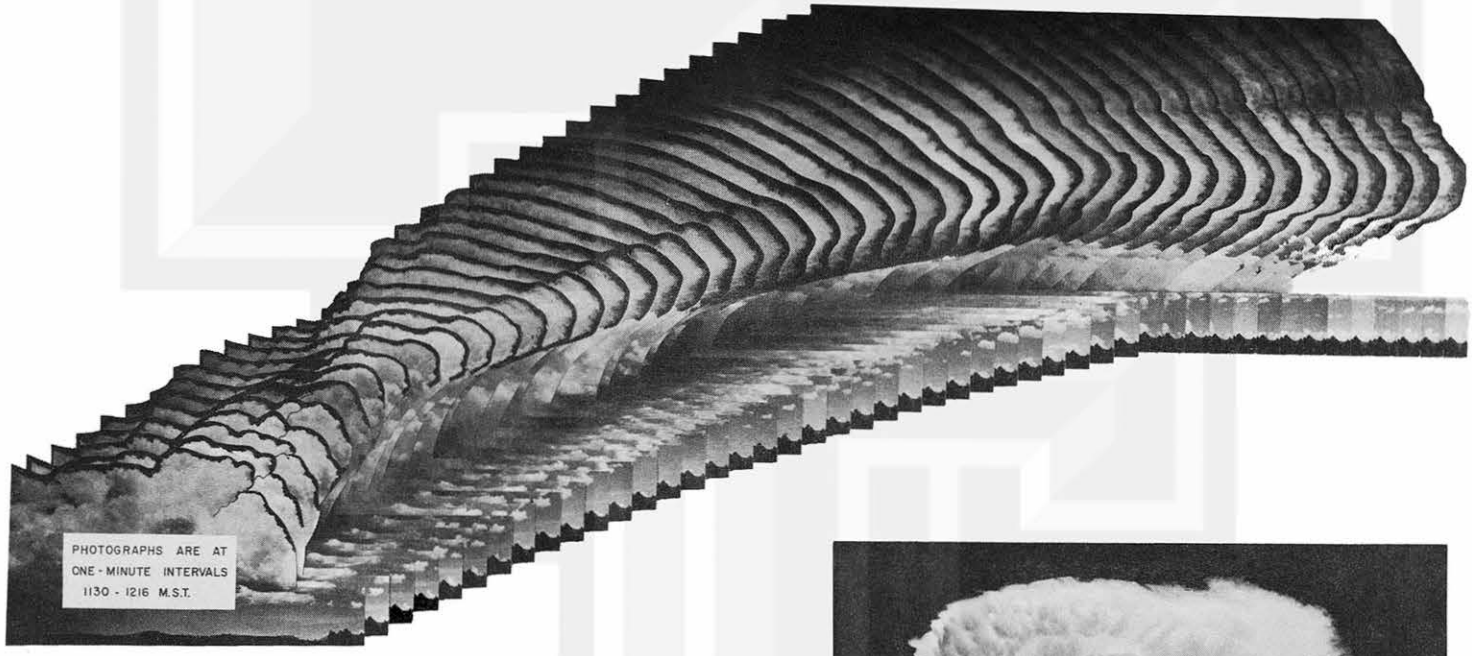

Fig. 23. Composite photograph showing congestus and cumulonimbus anvil growth at one-minute intervals from 1130 to 1216 MST.

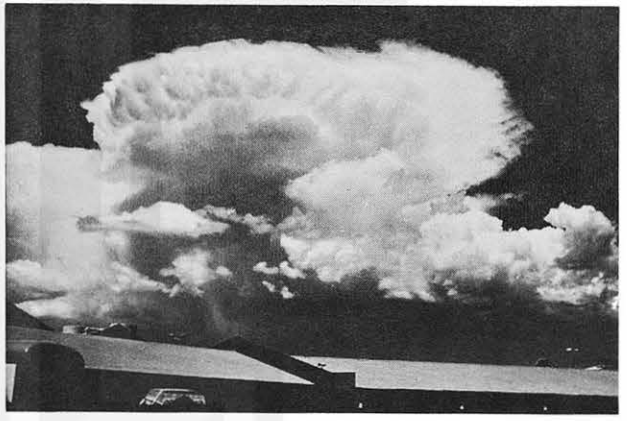

Fig. 24. Photograph taken from eastern part of Flagstaff showing entire cumulonimbus at 1150. A shaft of hail is seen falling from the left part of the cloud, but no rain is visible. Note the older cumulonimbus in the background to the left. Courtesy of P.H. Wyckoff, Armour Research Foundation.

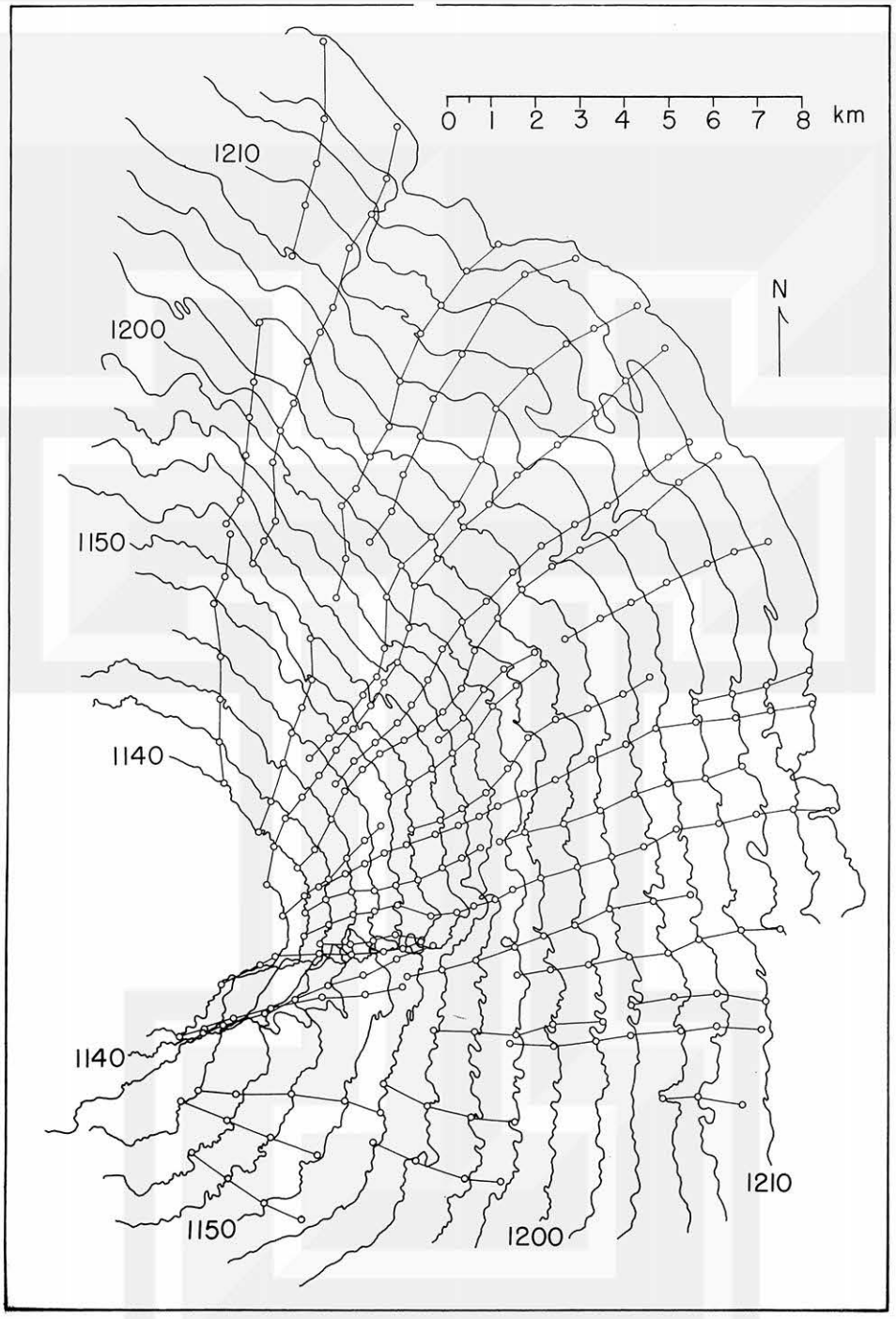

Fig. 25. Anvil outlines relative to the center of the cumulonimbus.

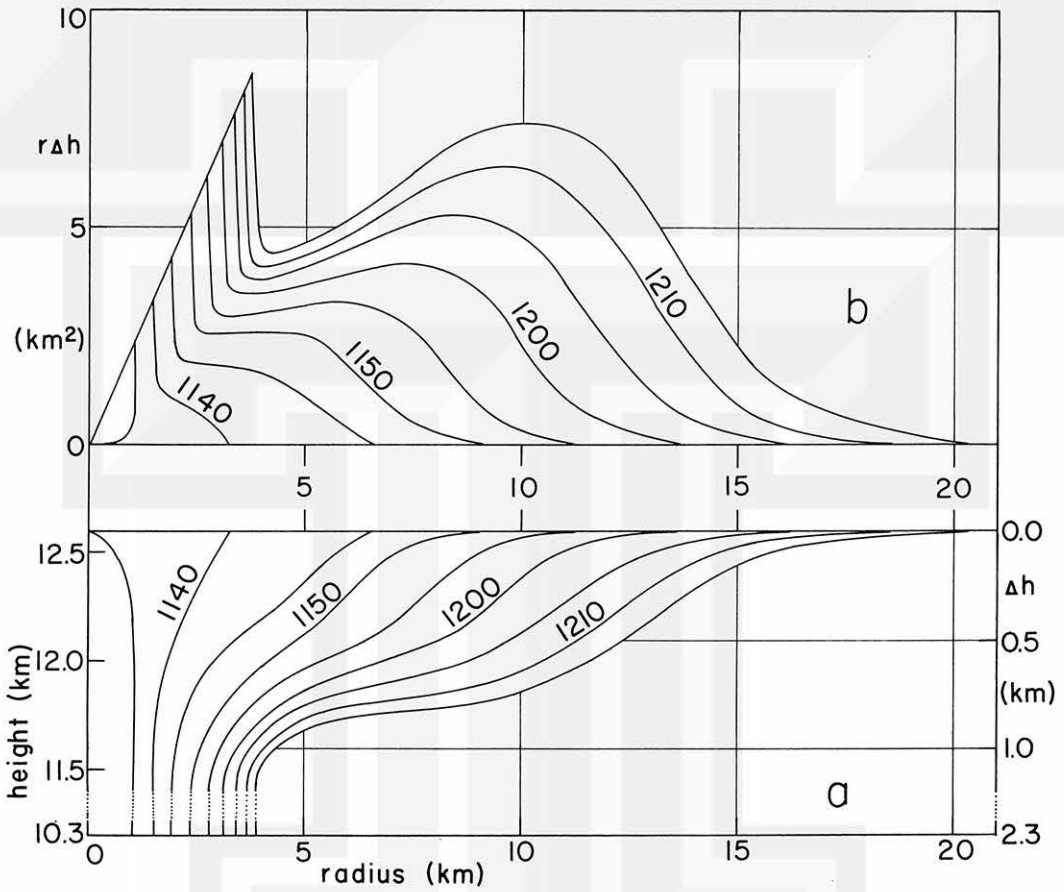

Fig. 26. a) Schematic outline of the anvil from 1135 to 1215. b) The product r Δ h as a function of radius that was used in integrating Eq. (17).

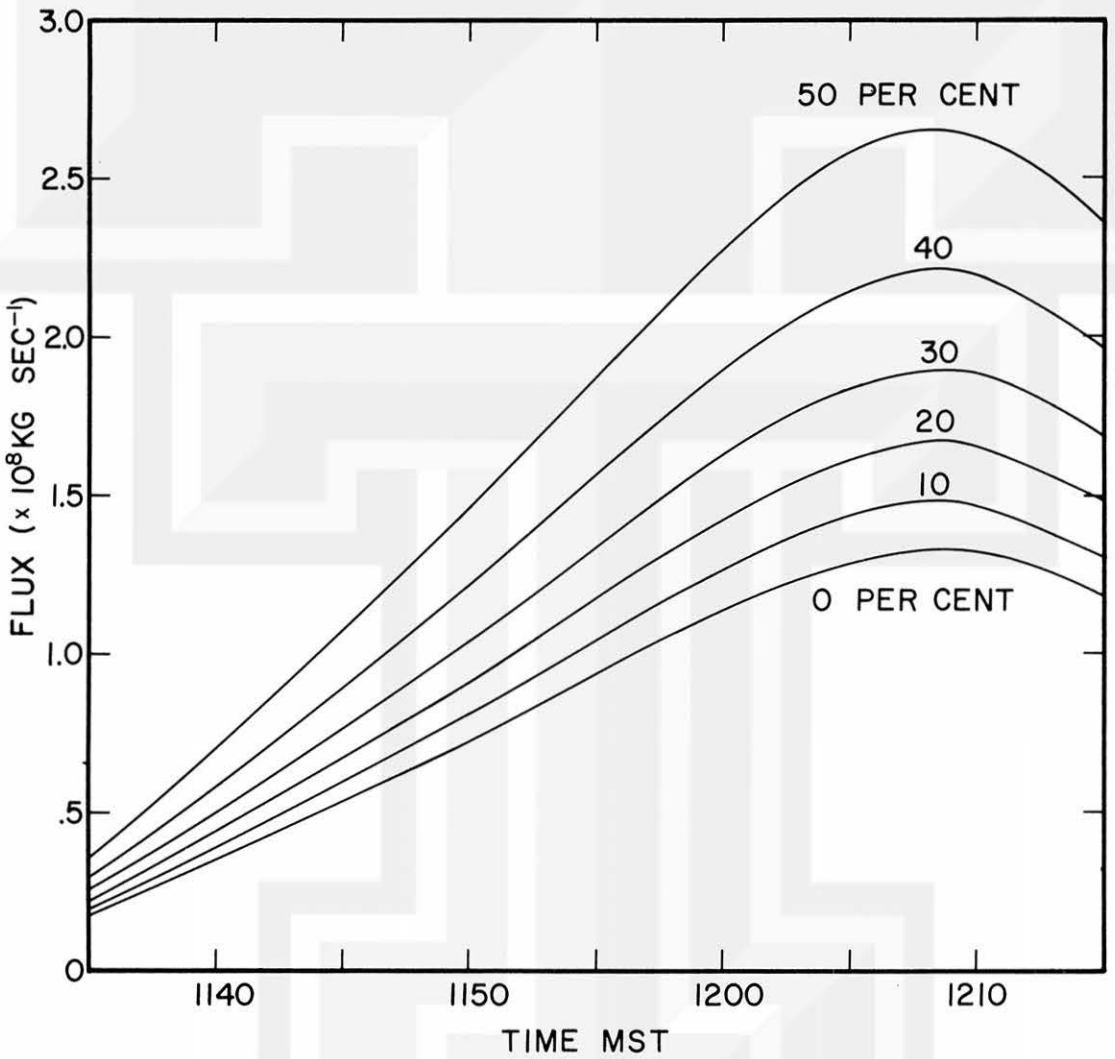

Fig. 27. Flux into the anvil based on various percentages of the air within the anvil passing through the sides of it at a given time.

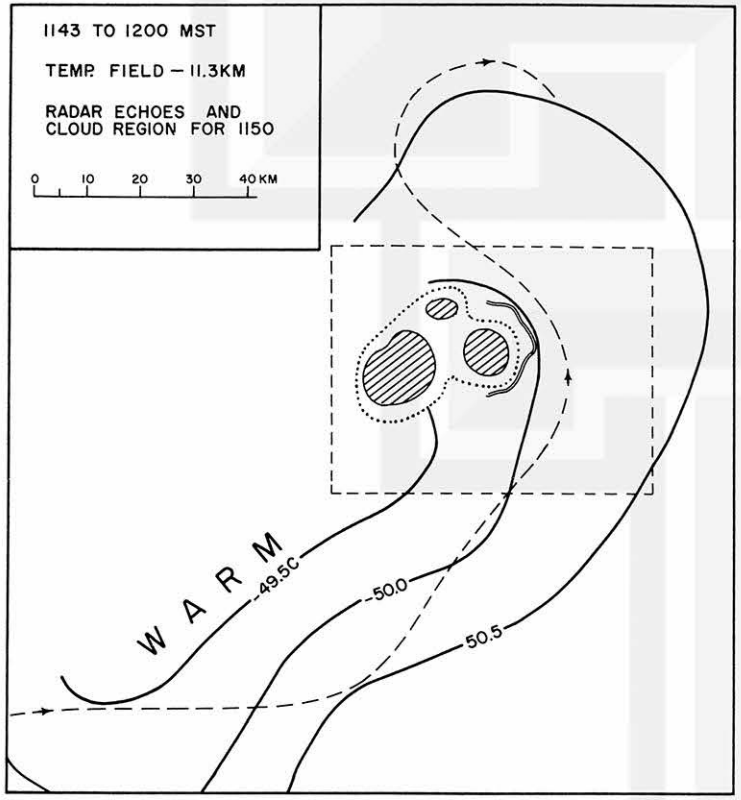

Fig. 28. Temperature field (solid lines) around the cumulonimbi as indicated by the aircraft's first pass (dashed line with arrows). Dotted curve outlines region of clouds. Dashed rectangle is same area as shown in Figs. 6 and 11-14. Double line is edge of anvil and shading represents radar echoes.

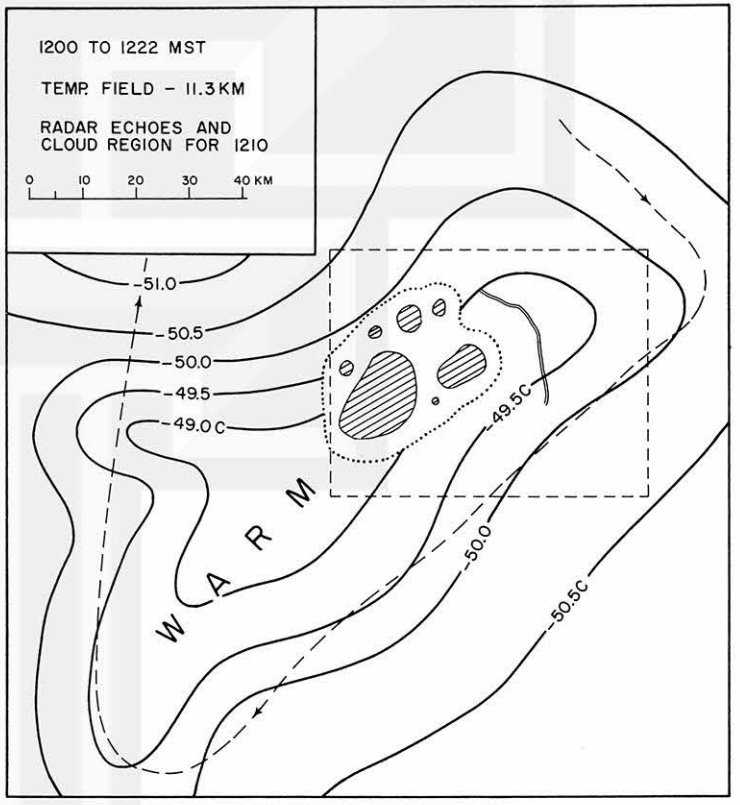

Fig. 29. Same as Fig. 28, but for second pass.

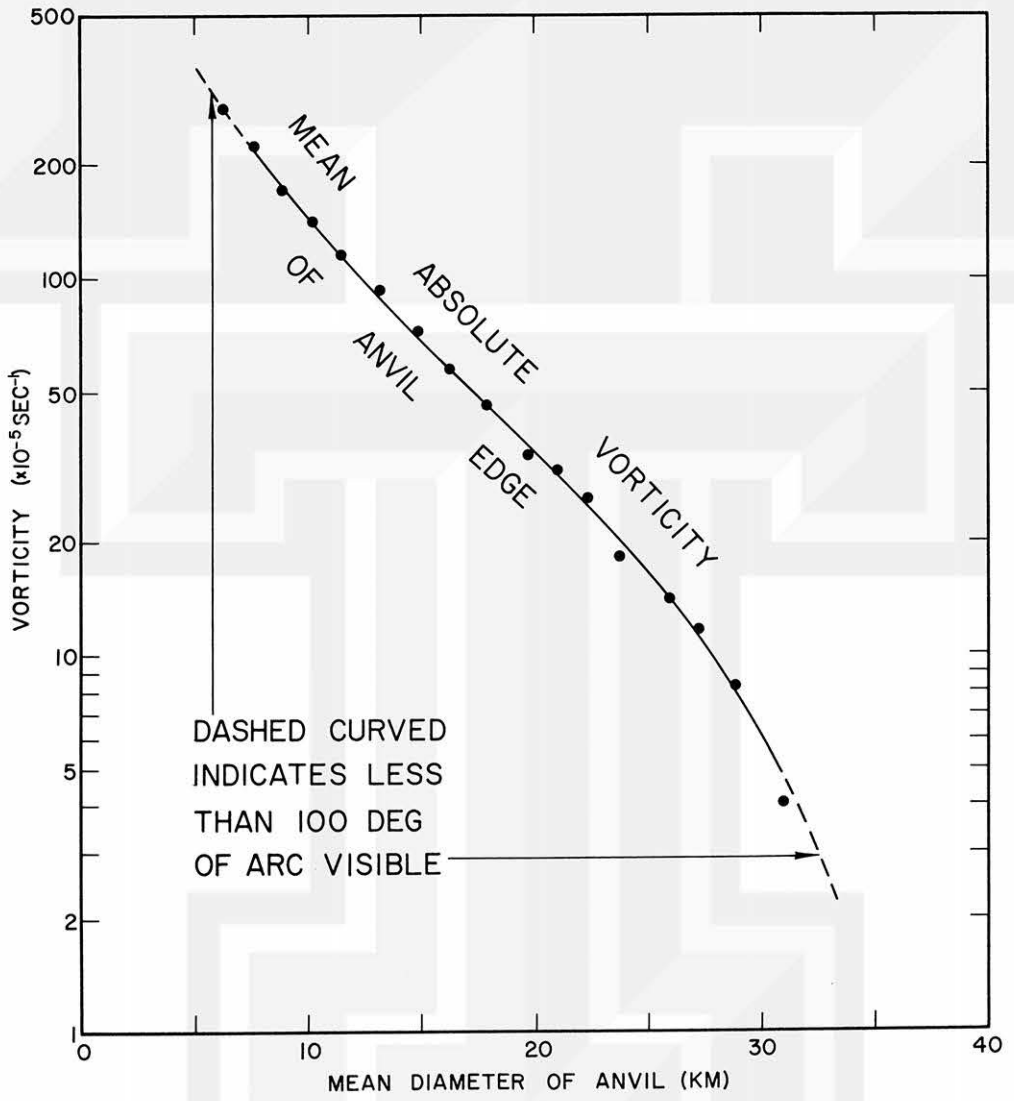

Fig. 30. Mean absolute vorticity measured along that part of the anvil's edge shown in Figs. 23 and 25.

6. Model of a Cumulonimbus Based on the Thermodynamic and Photogrammetric Analyses

The model presented here is of a cumulonimbus that consists entirely of an updraft. In order to be realistic it is necessary to restrict the discussion to the first five or ten minutes following the initial anvil formation; therefore, the remainder of this paper will be concerned only with the cloud as it appeared at 1145 MST.

The mean vertical velocity ($\overline{w}$) across the cloud at the level of maximum vertical velocity can be computed from the flux (F) in the following way:

$$\overline{w} = \frac{4F}{\pi \rho D^2} \qquad (19)$$

By applying this to the range of flux values in Fig. 27, where ρ is 0.42 kg m^{-3} and D is 4.0 km, the mean velocity ranges from 10 to 20 m sec^{-1}. The characteristic entrainment rate (see Fig. 2) for a cloud this size is 10 to 20 per cent $(100\ mb)^{-1}$; the resulting mean vertical velocities are approximately 21 to 25 m sec^{-1}. The disparity between the maximum vertical velocities obtained from the two independent procedures led the authors to devise a method that would produce more compatible results.

Three-region model of a thunderstorm. As an alternative to using one entrainment rate for an entire cloud, it was felt that it would be more realistic to approximate the cloud with three concentric regions - each one representing a different degree of mixing with the environment, i. e., each having a different entrainment rate. The outer portion would exhibit the greatest amount of mixing, the middle portion a lesser amount, and the center none. Therefore the vertical stem of the cumulonimbus has been approximated by three concentric cylinders. A similar concept has also been proposed by Houghton and Cramer (1951).

Under this new set-up, Eq. (13) had to be modified in order to determine the entrainment rate for a segment of a cloud. Since α is the ratio of the radial velocity to the vertical velocity, the following values of α were assigned to the outer, middle, and central regions - 1.0, 0.1, and 0, respectively. Therefore the equations for computing the entrainment rates in the three regions are:

$$E_1 = 4\beta \frac{D_1 - D_2}{D_1^2 - D_2^2} \quad , \qquad (20)$$

$$E_2 = 0.4\beta \frac{D_2 - D_3}{D_2^2 - D_3^2} \quad , \qquad (21)$$

and

$$E_3 = 0 \quad , \qquad (22)$$

where E_1 , E_2 , and E_3 are the entrainment rates in the outer, middle, and central regions, respectively, and where D_1 , D_2 , and D_3 are the diameters of the outermost portions of each region.

In (20) through (22), there is complete arbitrariness in the selection of D_2 and D_3 ; however, D_1 is fixed by observation and equal to 4.0 km. Also, the proper flux curve in Fig. 27 has not yet been determined. Since one or the other had to be fixed, it was assumed that 30 per cent of the updraft air passed through the visible anvil; this value led to a mean vertical velocity of 14.7 m sec^{-1} . Using Eq. (11), a series of trial-and-error calculations were made of the maximum vertical velocity for various diameters. The only requirements imposed on the results were that the mean vertical velocity be equal to 14.7 m sec^{-1} and that the step-like horizontal distribution approximates the following bell-shaped curve

$$w = exp\left[-\left(\frac{r}{r_o}\right)^2 \right] , \qquad (23)$$

where r ranges from 0 to 2 km and r_o is equal to 1 km. After numerous calculations, diameters of 2.4 km for D_2 and 1.6 km for D_3 finally gave the desired results. These diameters result in entrainment rates of $E_1 = 63\beta$ per cent $(100\ mb)^{-1}$ and $E_2 = 10\beta$ per cent $(100\ mb)^{-1}$. The fact that β increases with height is significant because the radial shear of the vertical motion increases up to the level of maximum vertical velocity; also, the divergence of the updraft in the anvil produces a great deal of turbulent mixing.

In Fig. 31 a schematic drawing of the cumulonimbus at 1145 is presented. The three-region model reveals that the middle region is significantly narrower than the other two; this is logical if one interprets the middle region as being a transition zone between the outer region where the inflowing air is mixing turbulently with the cloud and the center region where only vertical motions are present. Arrows are drawn in each of the three regions to show the direction (not the magnitude) of the flow for the appropriate values of α . The resulting streamlines reveal that the model is quite realistic.

Vertical- and radial-velocity distributions. Figure 32 reveals the cross section of vertical velocity within the updraft stage of a cumulonimbus; the values are based on the bell-shaped approximation to the computed results. It is noted that the maximum value is slightly greater than 30 m sec^{-1} . The outline of the anvil is the one observed at 1145 (Fig. 26); the relative diameters of the three sections were

maintained up to the top of the anvil. Contained within the dashed lines beneath the cloud is the approximate region of up-motion for converging air.

The radial velocity at various levels of the vertical stem of the cloud were computed from (12); the velocities as a function of radius are plotted in Fig. 33. The curves are labeled as the height above cloud base. In order to compare them with the vertical velocity, the levels at which they occur are indicated in Fig. 32 by horizontal dashed lines. In the lower portion of the cloud, the radial velocity of the converging air is 2 to 3 m sec^{-1} . Then the radial velocity decreases considerably at high levels as the vertical velocity becomes more nearly constant with height. Above the level of maximum vertical velocity the air becomes divergent.

Distribution of water content. The distribution of the water content within the cumulonimbus is presented in Fig. 34. The lines in the middle and bottom portions of the cloud are based on reliable data. However, above 11 km the information revealed from distributions similar to those in Fig. 3 was of no help in determining the distribution of the water content in the expanding anvil; so the lines that were drawn in the anvil region are speculative.

The amount of water substances found in a cloud depends to a great extent upon the amount of moisture in the environment. However, disregarding the environment of a sampled cloud, the water contents shown in Fig. 34 are compared with measured values. By taking an average of the values measured by Lewis (1947), Lewis and Hoecker (1949), Day and Murgatroyd (1953), and Day (1955), one would expect the mean water content in a cumulonimbus to be roughly 0.4 to 0.8 gm kg^{-1} and the maximum value to be in the range from 2 to 4 gm kg^{-1} ; all of these measurements were made with either rotating cylinders or icing discs. Using visibility as the criterion for the measure of liquid-water content, Weickmann and aufm Kampe (1953) obtained mean and maximum values of 2.8 and 11 gm kg^{-1} , respectively. While there is considerable discrepancy between the latter and former sets of values, the cloud presented here falls roughly in the middle: its mean value is approximately 2 gm kg^{-1} and the indicated area of maximum is nearly 5 gm kg^{-1} ; localized, smaller scale maxima could be considerably higher. Therefore, the water content in this model cumulonimbus is quite realistic.

Hydrostatic, non-hydrostatic, and total excess pressure. For a layer of stagnant air, the vertical distribution of pressure within it is completely described by the hydrostatic relation

$$\frac{dp_h}{dz} = -\rho g \quad , \tag{24}$$

where p_h is the hydrostatic pressure, ρ is the density, and g is the acceleration due to gravity. However, once the air is in motion (to be more exact - accelerating), a non-hydrostatic contribution to the pressure develops.

For the nearly steady-state conditions that exist in the updraft stage of a cumulonimbus, the vertical equation of motion can be written as

$$v_r \frac{\partial w}{\partial r} + w \frac{\partial w}{\partial z} = -\frac{1}{\rho} \frac{d}{dz}(p_h + \pi) - g, \qquad (25)$$

where π is the non-hydrostatic pressure. Substituting (24) into the right side of (25), the latter becomes

$$\frac{d\pi}{dz} = -\rho\left(v_r \frac{\partial w}{\partial r} + w \frac{\partial w}{\partial z}\right). \qquad (26)$$

The change in the total pressure, p, with height is obtained by combining (24) and (26),

$$\frac{dp}{dz} = -\rho\left(g + v_r \frac{\partial w}{\partial r} + w \frac{\partial w}{\partial z}\right). \qquad (27)$$

The pressure exerted on any surface is a consequence of the total influence of all of the air above that level. Therefore, the pressure at some level z can be expressed as

$$p(z) = p(\infty) - \int_{\infty}^{z} \rho\left(g + v_r \frac{\partial w}{\partial r} + w \frac{\partial w}{\partial z}\right) dz, \qquad (28)$$

where $p(\infty)$ can be considered as the pressure at the top of the atmosphere.

It is often convenient to consider pressure in a cloud as being an excess pressure (positive or negative) relative to the environment. If it is assumed that only negligible motions are induced by a spreading anvil on the air above it, then the air above the cloud shall have the same pressure as that above the environment, i.e., there would be zero excess pressure at the top of the cloud. Therefore, in terms of excess pressure, (28) can be expressed as

$$\Delta p(z) = -\int_{z_T}^{z} \left[g \Delta\rho + \rho\left(v_r \frac{\partial w}{\partial r} + w \frac{\partial w}{\partial z}\right)\right] dz, \qquad (29)$$

where $\Delta p(z)$ is the excess pressure at level z, z_T is the height of the top of the cumulonimbus, ρ is the cloud density, and $\Delta\rho$ is the excess (positive or negative)

of the cloud density over that of the environment. The approximation is made here that the environment is in hydrostatic equilibrium.

Using (29), the hydrostatic, non-hydrostatic, and total excess pressures were computed for the midpoints of each of the three regions in the model. The temperatures used in determining the densities were computed from (7). Figures 35a through c show the resulting vertical distributions of the excess pressures. It is noted that the hydrostatic and non-hydrostatic excess pressures are essentially 180^{o} out of phase.

An important fact revealed by the three figures is that for a cumulonimbus the non-hydrostatic excess pressure is always positive from the lower portions of the cloud to the ground. An inspection of the non-hydrostatic terms in (29) reveals that even when there is a downdraft in a cumulonimbus the non-hydrostatic excess pressure in the lower half of the cloud and below is positive, provided that

$$\left| w \frac{\partial w}{\partial z} \right| > \left| v_r \frac{\partial w}{\partial r} \right|.$$

Schaffer (1947), as an extension of Levine's (1942) work, theoretically determined that the non-hydrostatic excess pressure due to an updraft should be positive on the ground. He concluded that the excess pressure should be 0.2 to 0.5 mb.

The two papers cited above are part of an interesting controversy, which might be called the "Thunderstorm-High Controversy," that was started by Levine's (1942) paper and laster for ten years. The main participants were Buell (1943a and b), Mal and Rao (1945), Mull and Rao (1950), and Schaffer (1947, 1952). The initial attempts were to show that the high-pressure area associated with thunderstorms was caused by upward accelerating air. Since only the non-hydrostatic pressure was considered, positive excess pressure was obtained. But Mal and Rao (1945) theoretically showed that the non-hydrostatic excess pressure for an updraft should be negative at the ground. By referring to Fig. 35, one notes that $\Delta\pi$ should be positive on the ground even though the total excess pressure is negative. The later papers seem to have resolved the problem by considering the total excess pressure produced by both up- and downdrafts.

By combining the surface pressures from Figs. 35a through c, the pressure as would be seen on a microbarograph is drawn in Fig. 36. Since the pressure on the surface is the result of integrating from the top of the cloud, errors involved in the data also accumulate in the summing process. Therefore, the excess pressures on

the ground include an error of a few tenths of a millibar. This was taken into account when drawing the curves, especially through the points for the outer region. The pressure distribution for the total excess pressure beneath the developing cumulonimbus is realistic in both shape and magnitude.

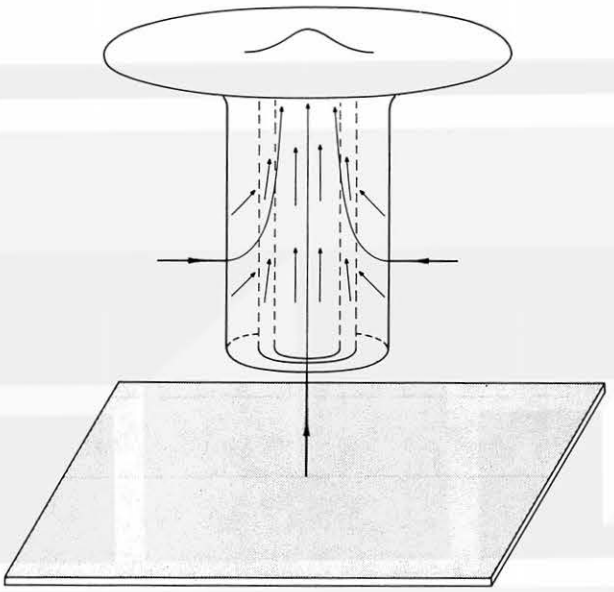

Fig. 31. Three-region model of the updraft stage of the cumulonimbus at 1145. Short arrows show wind direction for appropriate values of α . Heavy arrows show resulting wind flow.

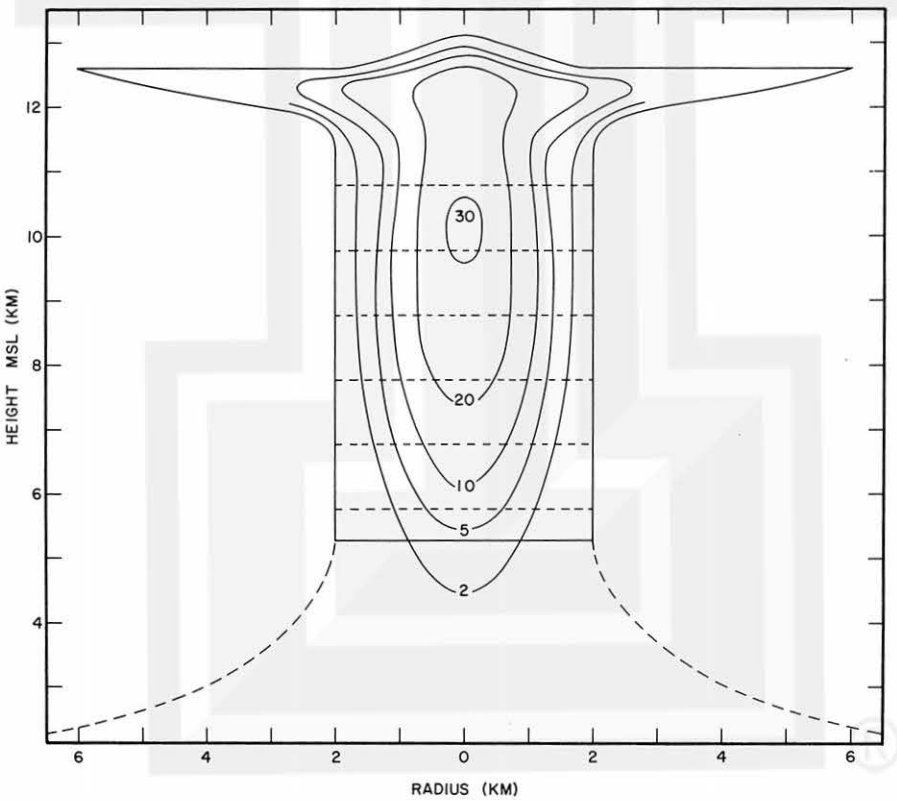

Fig. 32. Distribution of vertical velocity (m sec^{-1}) below and within the cumulonimbus at 1145. Dashed lines below the cloud indicate the approximate region where the converging wind has a vertical component. The horizontal dashed lines in the cloud represent the levels shown in Fig. 33.

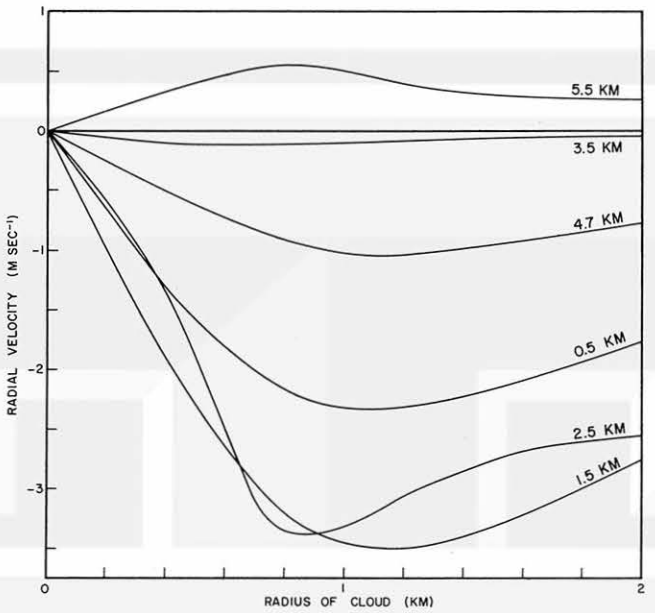

Fig. 33. Radial distribution of the radial velocity at various levels in the cloud. The curves are labeled as height above cloud base. Their relative locations within the cumulonimbus are indicated by dashed horizontal lines in Fig. 32.

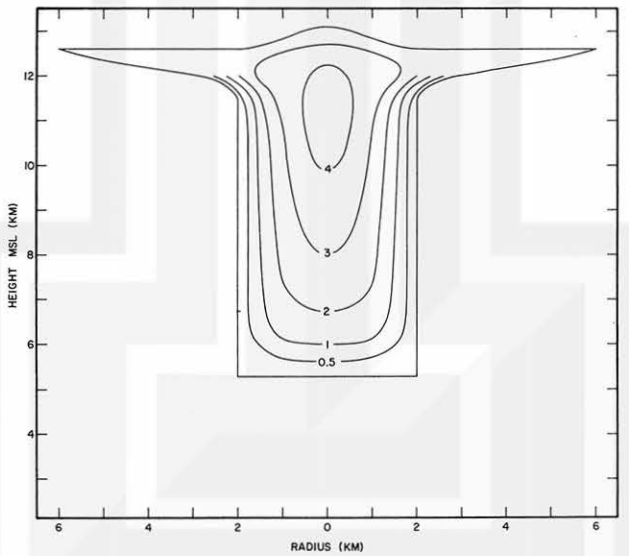

Fig. 34. Distribution of water content (gm kg^{-1}) within the cumulonimbus at 1145.

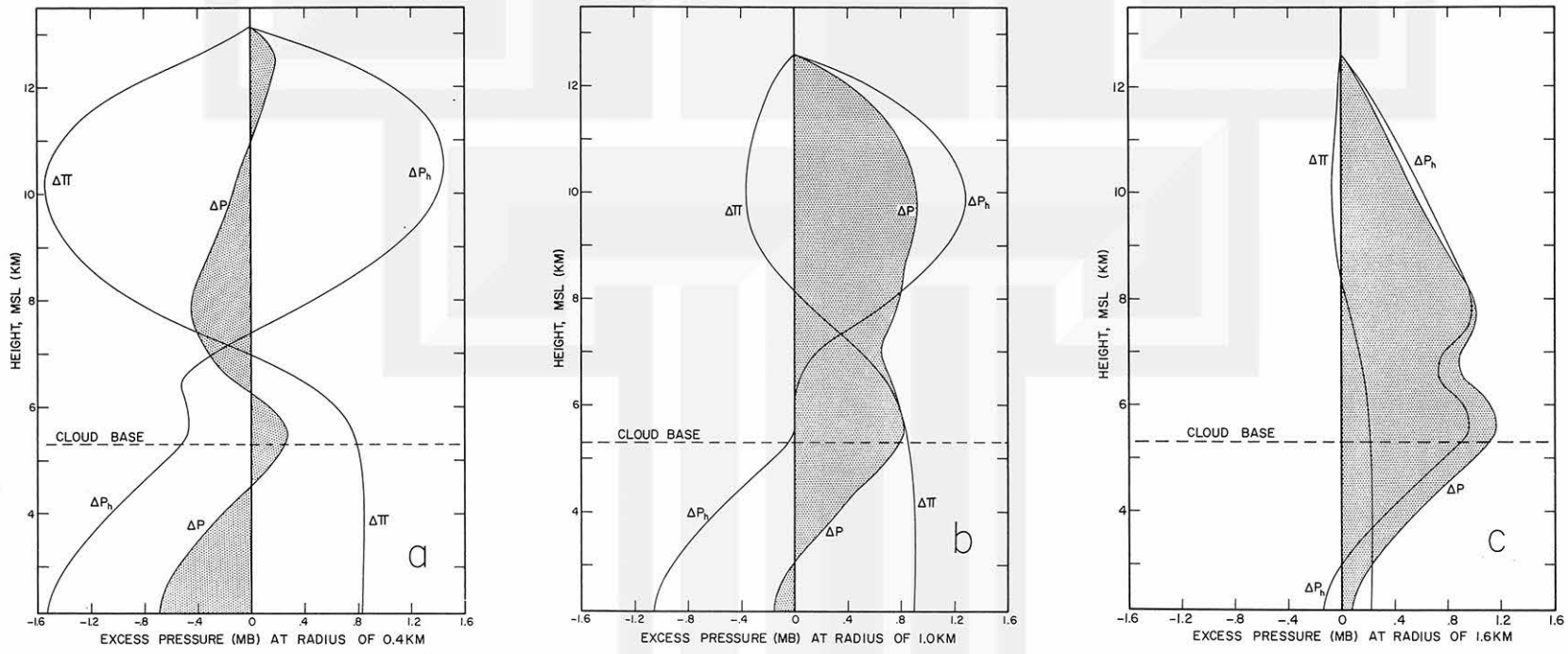

Fig. 35. Vertical distribution of hydrostatic, non-hydrostatic, and total excess pressures at radii of a) 0.4 km, b) 1.0 km, and c) 1.6 km. The shaded area represents the total excess pressure.

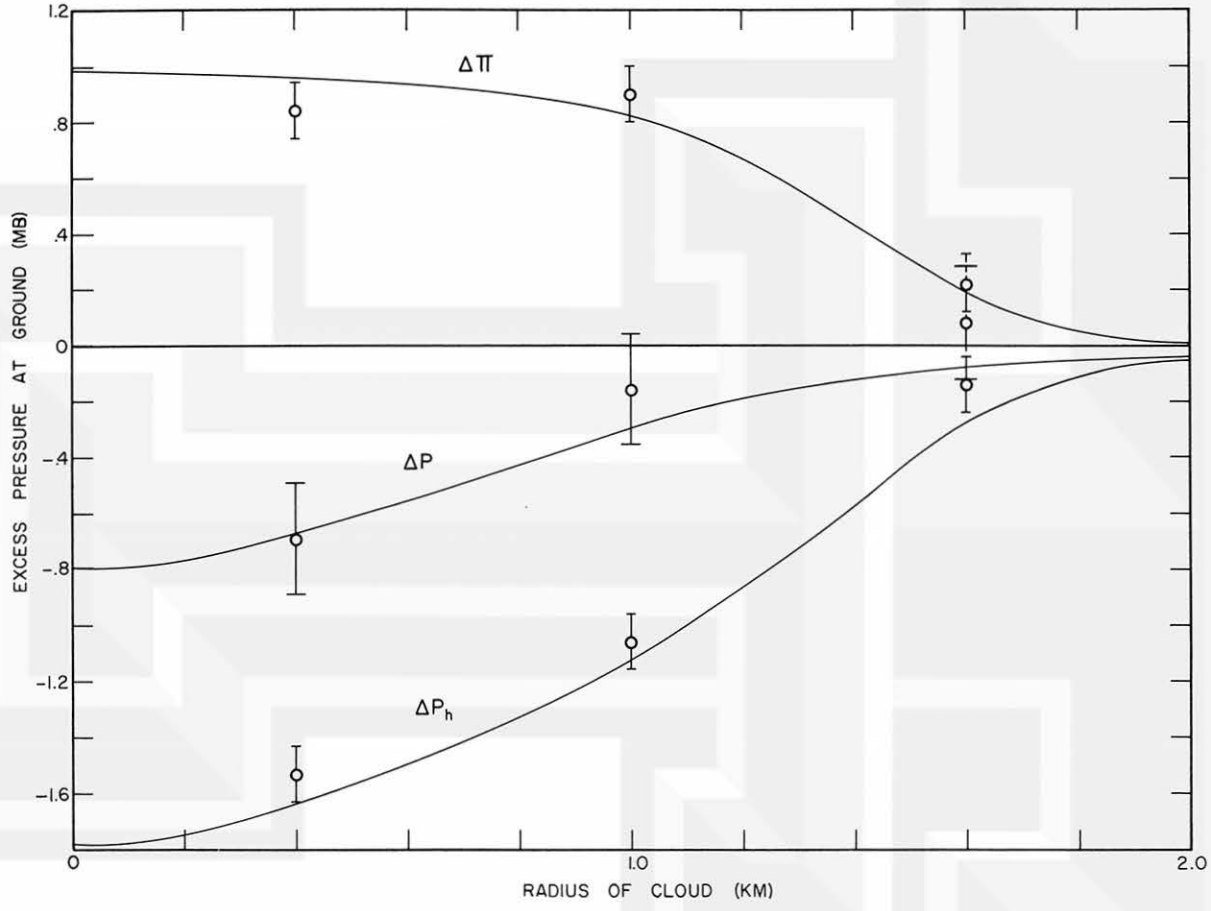

Fig. 36. Radial distribution of hydrostatic, non-hydrostatic, and total excess pressure on the ground. The data points were obtained from Fig. 35. The vertical lines represent ranges of 0.1 mb for hydrostatic and non-hydrostatic excess pressure and 0.2 mb for total excess pressure.

7. Evaluation of the Kinematic Eddy Viscosity Coefficient

Determination of ν_e by combining entrainment and viscosity processes. As pointed out earlier, the entrainment concept is an approximation of the turbulent exchange processes. In the previous section, the vertical velocity was computed from the equation

$$\frac{1}{2}\rho_2 w_2^2 = \frac{\frac{1}{2}\rho_1 w_1^2 + \bar{\rho}\Delta K}{1 + E\Delta p} . \qquad (11)$$

The equation that would have been employed had the exchange processes been used instead of entrainment is

$$\frac{1}{2}\rho_2 w_2^2 = \frac{1}{2}\rho_1 w_1^2 + \bar{\rho}\Delta K_1 + \bar{\rho}\,\nu_e \nabla^2 w \Delta z , \qquad (30)$$

where ΔK_1 is the change in kinetic energy per unit mass between levels 1 and 2 for an entrainment rate of 10 per cent $(100\ mb)^{-1}$, ν_e is the kinematic eddy viscosity coefficient, Δz is the vertical distance between the two levels, and ∇^2 is the Laplacian operator, such that

$$\nabla^2 w = \frac{\partial^2 w}{\partial r^2} + \frac{1}{r}\frac{\partial w}{\partial r} + \frac{\partial^2 w}{\partial z^2} . \qquad (31)$$

The value of 10 per cent $(100\ mb)^{-1}$ was used to represent a mean energy increment across the entire cloud; this may lead to small underestimates of the coefficient in the center of the cloud and overestimates near the edges.

In Eqs. (11) and (30) densities and vertical velocities are the same; the kinetic energy increment, ΔK_1, in (30) can be determined from Fig. 5. Rearrangement of the terms in (30) results in

$$\nu_e = \frac{\frac{1}{2}\left(\rho_2 w_2^2 - \rho_1 w_1^2\right) - \bar{\rho}\Delta K_1}{\bar{\rho}\,\nabla^2 w \Delta z} , \qquad (32)$$

where ρ_1 , ρ_2, $\bar{\rho}$, w_1 , w_2 , ΔK_1, and Δz are known and where $\nabla^2 w$ can be computed from (31). Equation (32) was evaluated at 66 grid points in a vertical cross section of the cloud - at radial increments of 0.4 km from the center outward and at 1-km increments in the vertical from 5.8 to 10.8 km. No computations were made in the anvil. The resulting values ranged from 1.7×10^2 to 2.0×10^4 $m^2\ sec^{-1}$; the distribution of the values are shown by the dashed curve in Fig. 38.

Comparison of the empirical ν_e with the theoretical K_z . Brown (1965) has proposed a set of theoretical equations for evaluating the turbulent exchange coefficients that include two significant modifications: 1) there is a different eddy viscosity coefficient for each of the three mutually orthogonal directions of motion and 2) the coefficients of eddy diffusion of heat and water vapor are combined into one equation. The eddy viscosity coefficient for vertical motion is defined as

$$K_z = \frac{\frac{1}{2} w^2}{\partial w / \partial r} \quad . \qquad (33)$$

Brown evaluated this equation for a simplified updraft model of a thunderstorm and obtained the range of values shown in Fig. 37.

Since (33) had not been evaluated using actual data, it was decided to use values from the same data points that were utilized in the evaluation of (32); K_z could not be computed along the center of the cloud due to the radial shear being zero. So K_z was evaluated at the other 60 data points. The distributions of both K_z and ν_e for the 60 points are shown in Fig. 38. The per cent frequency of points in each log cycle was plotted versus the mean viscosity coefficient in the respective cycle. The range of values for K_z were from 2.3×10 to 1.7×10^4 m^2 sec^{-1} ; the range in ν_e for 60 points was the same as 66 points. The simplified model used to construct Fig. 37 predicts a range in the order of magnitude from 10^2 to 10^4 m^2 sec^{-1} . The various values for the coefficient are summarized in Table 1.

Table 1. The range in the eddy viscosity coefficient for various methods of computation.

Equation	Eddy Viscosity Coefficient (m^2 sec^{-1}) Lowest	Median	Highest
Simplified model (Brown, 1965)	10^2	_____	10^4
K_z (60 points)	0.2×10^2	1.4×10^3	1.7×10^4
ν_e (60 points)	1.7×10^2	3.0×10^3	2.0×10^4
ν_e (66 points)	1.7×10^2	3.2×10^3	2.0×10^4

Even though K_z shows lower values than ν_e , (this could be due to the use of the mean ΔK_1 in (32)) there is reason to be greatly encouraged in that both (32) and (33) accurately determine the kinematic eddy viscosity coefficient to at least the proper order of magnitude. This confirms Kuo's (1962) statement that the entrainment concept and turbulent exchange processes are equivalent and gives much more credibility to the set of equations derived by Brown (1965).

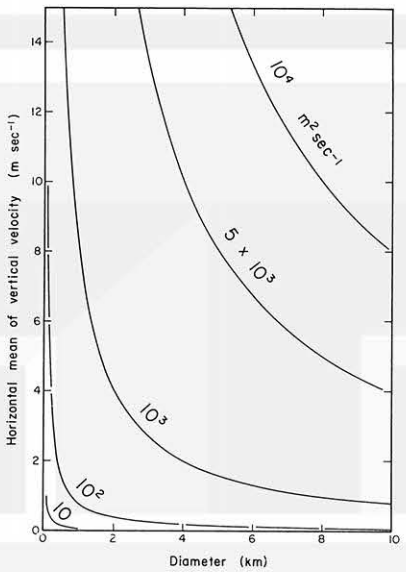

Fig. 37. Theoretical range in values of the kinematic eddy viscosity coefficient for vertical motion as a function of the horizontal mean of the vertical velocity at a given level and the diameter of the cloud at that level. From Brown (1965).

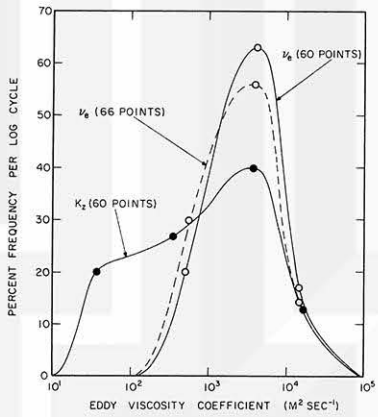

Fig. 38. Comparison of ν_e (empirical) and K_z (theoretical) at grid points within the vertical stem of the cumulonimbus. The additional six points used for the dashed curve were along the center of the cloud, where K_z is not defined. Each data point for the per cent frequency per log cycle is plotted at the value of the average viscosity coefficient for that cycle.

8. Conclusions and Summary

It has been shown that as cumuli grow in a series of pulsating steps into a cumulonimbus, the newer growths become increasingly efficient in converting energy released by condensation into kinetic energy of growth. This increase in efficiency has been expressed in terms of a decrease in the fractional amount of environmental mass that is mixed with the cloud mass.

In order to show not only how the rate of entrainment decreases as clouds become larger but also how various other parameters change during the eventual development of a thunderstorm, the results of this and previous studies have been summarized in Table 2. The table contains the summary for four different sized clouds: small cumulus, cumulus congestus, cumulus congestus to cumulonimbus (the size investigated in this paper), and large cumulonimbus. Values for the kinetic energy and water content are based on Figs. 3 and 5. The vorticity indicated for the smaller clouds are estimates not based on data.

Table 2. Various meteorological parameters associated with the four stages of development of cumuliform clouds.

Parameter	Small Cumulus	Cumulus Congestus	Congestus to Cumulonimbus	Large Cumulonimbus
Diameter (km)	1	2	4	10
Mean entrainment rate [per cent (100 mb)$^{-1}$]	100-200	25-100	10-25	< 10
Eddy viscosity coefficient (m^2 sec^{-1})	10^2	10^3	$5x10^3$	10^4
Flux (kg sec^{-1})	10^5 - 10^6	10^6 - 10^7	10^7 - 10^8	10^9
Maximum kinetic energy* per unit mass (m^2 sec^{-2})	<50	50-150	150-225	>225
Maximum water content* (gm kg^{-1})	<1.0	1.0-2.5	2.5-4.0	>4.0
Absolute vorticity of updraft (sec^{-1})	$\leq 10^{-5}$	10^{-4} - 10^{-3}	10^{-3} - 10^{-2}	$> 10^{-2}$

* = for environment similar to that found in northern Arizona

An important outcome of this study has been to present evidence of the rotating nature of cumulus congestus clouds that develop into the ordinary thunderstorm. Although vorticity measurements were not obtainable until after the anvil started to spread, the relatively high degree of rotation initially is a conclusive indication that the updraft within the cloud was rotating at rates of 10^{-3} to 10^{-2} sec^{-1} . This indicates that a rotating updraft should be an essential feature in kinematic models of both severe and non-severe thunderstorms.

While it is logical to assume that air in the anvil-shaped top of a cumulonimbus is expanding horizontally at a faster rate than the visible anvil, evidence has been presented to show that this is indeed the situation that exists. In fact it is so pronounced that temperature anomalies of nearly 2C caused by the descending air can be found about 1 km below the anvil. The effect of the outflow on a rawinsonde record has been shown.

The pressures recorded on the ground are sometimes difficult to interpret due to the combined effects of the hydrostatic and non-hydrostatic components that are produced at various levels above the ground. In this study, the wind density fields within and beneath the cumulonimbus were used to compute the distribution of the hydrostatic, non-hydrostatic, and total excess pressure. As is the case prior to the formation of a precipitation downdraft, the computations showed that a low-pressure area of nearly one millibar occurred beneath the cloud.

Since the entrainment concept approximates the actual turbulence that exists in a cloud, the velocities obtained from the entrainment calculations were used to compute the values of the eddy viscosity coefficient. The computed values ranged from 10^2 to 10^4 m^2 sec^{-1} ; they provided the first direct evidence of the reliability of the theoretical equation for the eddy viscosity coefficient for vertical motion proposed by Brown (1965). This theoretical equation and the rest of the proposed set should prove to be a valuable asset in future numerical modeling of clouds and larger circulations.

In the past, investigators have been content to use the entrainment concept to present a one-dimensional picture of the cumulonimbus. However, by making use of the proposed three-region model for the updraft stage, an axial-symmetrical three-dimensional cumulonimbus has been produced. This model is much more realistic since it allows the various parameters to vary across the cloud. Without the use of such a model, it would not have been possible to synthesize the photogrammetric and rawinsonde data into the workable form that was employed. The

realistic distributions of vertical and radial velocity, water content, surface pressure, and eddy viscosity coefficient that were produced attest to the validity of the model.

Acknowledgments:

The authors are indebted to Mr. Morton Glass of the Air Force Cambridge Research Laboratories for providing the photogrammetric data and making available the results of unpublished research. Mr. Joseph L. Goldman, now of the National Engineering Science Company, and Professor H.-L. Kuo of the University of Chicago provided helpful suggestions for various aspects of the research. The authors also wish to thank Mrs. Gisela L. Baralt and Miss Carrie Yokim for their valuable assistance throughout the course of this study.

REFERENCES

Ackerman, B., 1959: The variability of the water contents of tropical cumuli. J. Meteor., 16, 191-198.

Anderson, C. E., 1960: A study of the pulsating growth of cumulus clouds. Geophys. Res. Pap. No. 72, Air Force Cambridge Research Laboratories, Bedford, Mass., 136 pp.

Austin, J. M., 1948: A note on cumulus growth in a nonsaturated environment. J. Meteor., 5, 103-107.

_____, and A. Fleisher, 1948: A thermodynamic analysis of cumulus convection. J. Meteor., 5, 240-243.

Bjerknes, J., 1938: Saturated-adiabatic ascent of air through dry-adiabatically descending environment. Quart. J. R. Meteor. Soc., 64, 325-330.

Braham, R. R., Jr., 1952: The water and energy budgets of the thunderstorm and their relation to thunderstorm development. J. Meteor., 9, 227-242.

_____, 1963: Some measurements of snow pellet bulk-densities. J. Appl. Meteor., 2, 498-500.

Brown, R. A., 1965: On the determination of the exchange coefficients in convective clouds. SMRP Res. Paper 41, Univ. of Chicago, 7 pp.

Browning, K. A., 1964: Airflow and precipitation trajectories within severe local storms which travel to the right of the winds. J. Atmos. Sci., 21, 634-639.

_____, and R. J. Donaldson, Jr., 1963: Airflow and structure of a tornadic storm. J. Atmos. Sci., 20, 533-545.

Buell, C. E., 1943a: The determination of vertical velocities in thunderstorms. Bull. Amer. Meteor. Soc., 24, 94-95.

_____, 1943b: The determination of vertical velocities in thunderstorms (II). Bull. Amer. Meteor. Soc., 24, 211-212.

Bunker, A. F., 1953: Diffusion, entrainment and frictional drag associated with non-saturated, buoyant air parcels rising through a turbulent air mass. J. Meteor., 10, 212-218.

Byers, H. R., 1942: Nonfrontal thunderstorms. Misc. Rep., No. 3, Meteor. Dept., Univ. of Chicago, 26 pp.

_____, and E. C. Hull, 1949: Inflow patterns of thunderstorms as shown by winds aloft. Bull. Amer. Meteor. Soc., 30, 90-96.

Chou, H.-P., 1962: K voprosu o razvitii kuchevykh oblakov. [Development of cumulus clouds] . Akad. Nauk SSSR, Izv., Ser. Geofiz., No. 4, 548-557. Also translated into English in the corresponding issue of its Bull. Acad. Sci. USSR, Geophys. Ser., Wash., D. C.

Christians, H., 1935: Zur dynamik der cumuluswolke. [The dynamics of cumulus clouds] . Beitr. Physik Fr. Atmos., 22, 149-160. Also available as Amer. Meteor. Soc. translation T-G-155 through Library of Congress.

Day, G. J., 1955: A refrigerated disc icing meter. G. B. Air Ministry MRP, 916.

_____, and R. J. Murgatroyd, 1953: The cumulus cloud investigations made by Meteorological Research Flight during the period August 4th - 15th, 1952. G. B. Air Ministry MRP, 826.

Diem, M., 1948: Messungen der grösse von Wolkenelementen, II. [Measurements of the sizes of cloud elements, II] . Meteor. Rundschau, 1, 261-273.

Dufour, L., 1956a: Thermodynamical study of the entrainment of air into a cumulus. Tellus, 8, 202-205.

_____, 1956b: Entraînement d'air humide saturé contenant de l'eau liquide dans une masse d'air humide saturé contenant de l'eau liquide. [Entrainment of saturated air containing liquid water into a mass of saturated air containing liquid water]. Tellus, 8, 403-407.

Fujita, T., 1951: Micro-analytical study of thunder-nose. Geophys. Mag., Tokyo, 22, 71-88.

_____, 1958: Mesoanalysis of the Illinois tornadoes of 9 April 1953. J. Meteor., 15, 288-296.

_____, 1960: A detailed analysis of the Fargo tornadoes of June 20, 1957. Res. Paper No. 42, U. S. Weather Bureau, Washington, D. C., 67 pp.

_____, 1963: Analytical mesometeorology: A review. Meteor. Monogr., 5, No. 27, 77-125.

_____, 1965: Formation and steering mechanisms of tornado cyclones and associated hook echoes. Mon.Wea. Rev., 93, 67-78.

_____, K. A. Styber, and R. A. Brown, 1962: On the mesometeorological field studies near Flagstaff, Arizona. J. Appl. Meteor., 1, 26-42.

Glass, M., and T. N. Carlson, 1963: The growth characteristics of small cumulus clouds. J. Atmos. Sci., 20, 397-406.

Gutman, L. N., 1961: K teorii kuchevoĭ oblachnosti. [The theory of cumulus cloudiness] . Akad. Nauk SSSR, Izv., Ser. Geofiz., No. 7, 1040-1057. Also translated into English in the corresponding issue of its Bull. Acad. Sci. USSR, Geophys. Ser., Wash., D. C.

Haltiner, G. J., 1959: On the theory of convective currents. Tellus, 11, 4-15.

_____, and E. M. Chase, 1960: Some further results on convective currents. Tellus, 12, 393-398.

Hamilton, J. W., 1958: Some features in the use of radar in forecasts and warnings of heavy hail, damaging winds and/or tornadoes. Proc. Seventh Wea. Radar Conf., Boston, Amer. Meteor. Soc., Sec. H, 18-25.

Hoecker, W. H., Jr., 1957: Abilene, Texas, area tornadoes and associated radar echoes of May 27, 1956. Proc. Sixth Wea. Radar Conf., Boston, Amer. Meteor. Soc., 143-150.

Houghton, H. G., and H. E. Cramer, 1951: A theory of entrainment in convective currents. J. Meteor., 8, 95-102.

Kuo, H.-L., 1962: On the controlling influences of eddy diffusion on thermal convection. J. Atmos. Sci., 19, 236-243.

Levine, J., 1942: The effect of vertical accelerations on pressure during thunderstorms. Bull. Amer. Meteor. Soc., 23, 52-61.

Lewis, W., 1947: A flight investigation of the meteorological conditions conducive to the formation of ice on airplanes. U.S.N.A.C.A. Tech. Note No. 1393.

Lewis, W., and W. H. Hoecker, 1949: Observations of icing conditions encountered in flight during 1948. U.S.N.A.C.A. Tech. Note No. 1904.

Lilly, D. K., 1962: On the numerical simulation of buoyant convection. Tellus, 14, 148-172.

List, R., 1958: Kennzeichen atmosphärischen eispartikeln, 1 teil. [Characteristics of atmospheric ice particles, Part 1]. Z. Angew. Math. Phys., 9, 180-192.

Mal, S., and Y. P. Rao, 1945: Effect of vertical acceleration on pressure during thunderstorms. Quart. J. R. Meteor. Soc., 71, 419-421.

Malkus, J. S., 1954: Some results of a trade-cumulus cloud investigation. J. Meteor., 11, 220-237.

_____, and R. T. Williams, 1963: On the interaction between severe storms and large cumulus clouds. Meteor. Monogr., 5, No. 27, 59-64.

Mason, B. J., and R. Emig, 1961: Calculations of the ascent of a saturated buoyant parcel with mixing. Quart. J. R. Meteor. Soc., 87, 212-222.

Mei-Yuan, H., 1963: [Microstructure of cumulus clouds] . Akad. Nauk SSSR, Izv., Ser. Geofiz., No. 2, 362-376. Also translated into English in the corresponding issue of its Bull. Acad. Sci. USSR, Geophys. Ser., Washington, D. C., 225-233.

Morton, B. R., 1959: The ascent of turbulent forced plumes in a calm atmosphere. Int. J. Air Poll., 1, 184-197.

Mull, S., and Y. P. Rao, 1950: Dynamics of thunderstorms, Part 1. Indian J. Meteor. Geophys., 1, 116-136.

Newton, C. W., 1960: Hydrodynamic interactions with ambient wind field as a factor in cumulus development. Cumulus Dynamics, Proc. First Conf. on Cumulus Conv., New York, Pergamon Press, 135-144.

Ogura, Y., 1963: The evolution of a moist convective element in a shallow, conditionally unstable atmosphere: A numerical calculation. J. Atmos. Sci., 20, 407-424.

Prandtl, L., and O. G. Tietjens, 1934: Applied hydro- and aeromechanics. New York, McGraw-Hill, 311 pp.

Priestley, C.H.B., 1959: Turbulent transfer in the lower atmosphere. Chicago, Univ. of Chicago Press, 130 pp.

Richardson, L. F., 1921: Some measurements of atmospheric turbulence. R. Soc. London, Phil. Trans., Ser. A. 221, 1-28.

Ricou, F. P., and D. B. Spalding, 1961: Measurements of entrainment by axisymmetrical turbulent jets. J. Fluid Mech., 11, 21-32.

Schaffer, W., 1947: The thunderstorm high. Bull. Amer. Meteor. Soc., 28, 351-355.

_____, 1952: Second note on the thunderstorm high. Bull. Amer. Meteor. Soc., 33, 150-152.

Schmidt, F. H., 1947: Some speculations on the resistance to the motion of cumuliform clouds. Meded. Verh. (B), 1, No. 8, K. Ned. Meteor. Inst., 55 pp.

Schurz, D. R., and E. Persson, 1964: Computer programs for the reduction of photogrammetric cloud data. AFCRL-64-683, Final Rep., Contract AF 19(604)-4973. Dept. Civil Eng., Mass. Inst. Tech.

Squires, P., 1958: The spatial variation of liquid water and droplet concentration in cumuli. Tellus, 10, 372-380.

_____, 1962: The dynamics of clouds. In Fletcher, N. H., 1962: The physics of rainclouds. Cambridge, Cambridge Univ. Press, 1-30.

_____, and J. S. Turner, 1962: An entraining jet model for cumulo-nimbus updraughts. Tellus, 14, 422-434.

Stommel, H., 1947: Entrainment of air into a cumulus cloud. J. Meteor., 4, 91-94.

_____, 1951: Entrainment of air into a cumulus cloud II. J. Meteor., 8, 127-129.

Todd, C. J., 1964: Aircraft traverses in a growing mountain cumulus cloud. J. Atmos. Sci., 21, 529-538.

Weickmann, H. K., and H. J. aufm Kampe, 1953: Physical properties of cumulus clouds. J. Meteor., 10, 204-211.

Zaitsev, V. A., 1950: Vodnost' i raspredelenie kapel' v kuchevykh oblakakh. [Liquid water content and distribution of drops in cumulus clouds] . Trudy Glavnoi Geofiz. Observ., No. 19 (81), 122-132. Also available as Technical Translation TT-395 of the National Research Council of Canada, Ottawa, 1953, 21 pp.

MESOMETEOROLOGY PROJECT - - - - - RESEARCH PAPERS

(Continued from front cover)

16. Preliminary Result of Analysis of the Cumulonimbus Cloud of April 21, 1961 -Tetsuya Fujita and James Arnold

17. A Technique for Precise Analysis of Satellite Photographs - Tetsuya Fujita

18. Evaluation of Limb Darkening from TIROS III Radiation Data - S.H.H. Larsen, Tetsuya Fujita, and W. L. Fletcher

19. Synoptic Interpretation of TIROS III Measurements of Infrared Radiation -Finn Pedersen and Tetsuya Fujita

20. TIROS III Measurements of Terrestrial Radiation and Reflected and Scattered Solar Radiation - S.H.H. Larsen, Tetsuya Fujita, and W.L. Fletcher

21. On the Low-level Structure of a Squall Line - Henry A. Brown

22. Thunderstorms and the Low-level Jet - William D. Bonner

23. The Mesoanalysis of an Organized Convective System - Henry A. Brown

24. Preliminary Radar and Photogrammetric Study of the Illinois Tornadoes of April 17 and 22, 1963 - Joseph L. Goldman and Tetsuya Fujita

25. Use of TIROS Pictures for Studies of the Internal Structure of Tropical Storms -Tetsuya Fujita with Rectified Pictures from TIROS I Orbit 125, R/O 128 -Toshimitsu Ushijima

26. An Experiment in the Determination of Geostrophic and Isallobaric Winds from NSSP Pressure Data - William Bonner

27. Proposed Mechanism of Hook Echo Formation - Tetsuya Fujita with a Preliminary Mesosynoptic Analysis of Tornado Cyclone Case of May 26, 1963 -Tetsuya Fujita and Robbi Stuhmer

28. The Decaying Stage of Hurricane Anna of July 1961 as Portrayed by TIROS Cloud Photographs and Infrared Radiation from the Top of the Storm -Tetsuya Fujita and James Arnold

29. A Technique for Precise Analysis of Satellite Data, Volume II - Radiation Analysis, Section 6. Fixed-Position Scanning - Tetsuya Fujita

30. Evaluation of Errors in the Graphical Rectification of Satellite Photographs -Tetsuya Fujita

(Continued on outside)

MESOMETEOROLOGY PROJECT - - - - - RESEARCH PAPERS

(Continued from inside)

31. Tables of Scan Nadir and Horizontal Angles - William D. Bonner

32. A Simplified Grid Technique for Determining Scan Lines Generated by the TIROS Scanning Radiometer - James E. Arnold

33. A Study of Cumulus Clouds over the Flagstaff Research Network with the Use of U-2 Photographs - Dorothy L. Bradbury and Tetsuya Fujita

34. The Scanning Printer and Its Application to Detailed Analysis of Satellite Radiation Data - Tetsuya Fujita

35. Synoptic Study of Cold Air Outbreak over the Mediterranean Using Satellite Photographs and Radiation Data - Aasmund Rabbe and Tetsuya Fujita

36. Accurate Calibration of Doppler Winds for their Use in the Computation of Mesoscale Wind Fields - Tetsuya Fujita

37. Proposed Operation of Instrumented Aircraft for Research on Moisture Fronts and Wake Depressions - Tetsuya Fujita and Dorothy L. Bradbury

38. Statistical and Kinematical Properties of the Low-Level Jet Stream - William D. Bonner

39. The Illinois Tornadoes of 17 and 22 April 1963 - Joseph L. Goldman

40. Resolution of the Nimbus High Resolution Infrared Radiometer - Tetsuya Fujita

41. On the Determination of the Exchange Coefficients in Convective Clouds - Rodger A. Brown

42. A Study of Factors Contributing to Dissipation of Energy in a Developing Cumulonimbus - Rodger A. Brown and Tetsuya Fujita